Seismic Reliability Analysis of Long-Span Single-Pylon Suspension Bridge Subject to Nonstationary Ground Motions

Jin Zhang
Chengdu University of Technology
gang wang (wanggang@cdut.edu.cn)
State Key Laboratory of Geohazard Prevention and Geoenvironment Protection
Zhi-qiang Chen
Southwest Jiaotong University
Zhen-yu Yang
Chengdu University of Technology
Xing-hu Shi
Sichuan Highway Engineering Consult
Ming-zhi Xie
Southwest Jiaotong University

Research Article

Keywords: Seismic reliability analysis, Single-pylon suspension bridge, Maximum entropy method, Correlation reduced Latin hypercube sampling method, Unequal weights

Posted Date: March 18th, 2022

DOI: https://doi.org/10.21203/rs.3.rs-1448303/v1

Abstract

To efficiently and accurately evaluate the critical seismic response extreme value distribution (EVD) and seismic reliability analysis (SRA) of complex non-linear structures under nonstationary ground motions, a novel method for obtaining fractional moments via unequal weights combined improved correlation-reduced Latin hypercube sampling method (ICLHS) was proposed in this investigation. First, the basic theoretical methods of SRA were presented including dimension reduction simulation of nonstationary ground motions, single-loop maximum entropy theory of fractional moments, along with ICLHS for abtaining the fractional moments. Then, an effective structural seismic reliability assessment framework of complex nonlinear structures under nonstationary ground motions was built considering the double uncertainties of structural variables and seismic ground motions. and a three-story nonlinear shear frame structure was employed to verify the effectiveness of the proposed method. Finally, Based on the proprosed method and OpenSees finite element platform, the SRA of a typical long-span single-pylon suspension bridge was carried out and some critical conclusions were drawn.

1. Introduction

Seismic reliability analysis (SRA) of complex structure aims to estimate the failure probability of the system based on certain performance indicators considering the randomness of the seismic ground motions and structural uncertainties. On the one hand, due to the nonstationary and spatial correlation characteristics of ground motions [1], the amplitude, duration, and frequency components always show a large degree of change, and the random simulation of ground motions is a complicated process. On the other hand, the material and mechanical properties, geometric dimensions, as well as boundary conditions modeling of the structures are also uncertain. Further more, the seismic performance of the structures under seismic ground motions often shows a strong nonlinearity, and this nonlinearity will also be coupled with the the existing structural uncertainties. Therefore, the seismic reliability analysis considering the randomness of seismic ground motions and structural parameters uncertainty is an critical issue for the structural safety evaluation.

To solve the above challenge in SRA of structures, the stochastic vibration method and stochastic finite element method have been developed for structural dynamic reliability analysis [2–3]. The stochastic vibration method is mainly used to deal with randomness in the simulation of ground motions inputs. and although pseudo-excitation methods [4–5], the equivalent linearization method [6], the tail-equivalent linearization method [7], the FPK equation method [8], as well as the probability density evolution method [9–10] have been developed to solve the SRA of engineering structures, at present, the SRA of the complex nonlinear structures under nonstationary ground motions are still open challenges. Stochastic finite element method (SFEM) is mainly used to deal with structural parameter uncertainty analysis and has been developed to model the variability of structural parameters, such as the stochastic regression method [11], the orthogonal polynomial expansion method [12–13], the path integral method [14–15] as well as the dimensionality reduction method [16]. However, the estimation of the high-order statistics of the nonlinear seismic response of complex structures is a troublesome topic due to the multi-dimensional uncertainty of

the structural parameters and the randomness of ground motions. The Monte Carlo simulation (MCS) method [17] and its variants [18–20] deal with structural nonlinearities in random variables independent of dimensionality, but the time-consuming of SRA is unacceptable in application to real complex engineering structures.

The extreme value distribution (EVD), which is closely related to the first exceedance probability, is another effective method for reliability assessment [21]. According to the equivalent extreme value event proposed by Li et al [22], the failure probability of a structure can be assessed deterministically employing the inherent dynamic response information. Therefore, how to accurately obtain the EVD of the structural response is crucial to the evaluation of small probability events. Since fractional moments contain a large amount of higher-order integer moment information, the method of obtaining EVD by the fractional moment maximum entropy method (FM-MEM) has received much attention from scholars. However, for complex M-DOF structures, obtaining the EVD of the response by FM-MEM inevitably involves the solution of multi-dimensional integrals. In recent years, the methods applied to the calculation of multi-dimensional integrals can be divided into correlation sampling methods and cubature formulae [23]. In addtional, the correlation sampling methods are widely used in the computation of high-dimensional integrals due to their dimension-independent application and their good applicability to the nonlinear case [24–26]. However, these methods usually adapt equal weights when dealing with point weights to compute statistical moments, which is simple but computationally expensive for large nonlinear structures. On the other hand, cubature formulae usually refer to the determination of a specific weight values based on a series of functions, which are then weighted and summed as an approximation to a high-dimensional integral, such as Gaussian product methods and sparse lattices [27–28]. When the product function is smooth and oscillation-free, relatively accurate results can be obtained with fewer points in the cubic formulation. However, the response functions of complex nonlinear structures are often implicit functions, which are almost impossible to obtain in terms of access. Typically, seismic response of bridges with multi-degree-of-freedom and non-linearities involves high-dimensional random variables and implicit response functions, and it is more efficient to use correlation sampling methods to determine the structural uncertainty parameters. Recently, Shields et al [29] established a Latin partially stratified sampling method (LPSS) based on probability space decomposition, which improves the efficiency of simple random sampling and shrinks the sampling variance. However, for LPSS, fewer sampling points may still be pseudo-correlated and form local clusters, leaving the overall probability space potentially unextracted [30], such that fractional moments processed with equal weights can produce spurious EVD tail information. Considering the advantages and limitations of the sampling method and the cubic formula, it is a good strategy to combine the fractional moments with unequal weights based on the correlation sampling method with fewer sampling points to improve the accuracy and efficiency of the calculation [23].

As mentioned above, the SRA of complex non-linear bridge structures is still an open challenge. In previous studies, the influence of epistemic uncertainty (i.e., numerical modelling uncertainty) is often not taken into account [31–32], but the combination of ground motion randomness and structural parameter randomness has been proved to be very necessary [33–34]. In order to develop an efficient SRA framework considering double uncertainties of ground motions and structural parameters. First, based on improved

correlation-reduced Latin hypercube sampling method (ICLHS), the central L2 discrepancy orientation with higher efficiency is combined with ICLHS to extract structural uncertainty parameters [34]. Then, to reduce the bias caused by local clusters in the calculation of fractional moments with equal weights of integration points, fractional moments are calculated by constructing unequal weights on the integration points generated by ICLHS, which is a weighted sum of a set of deterministic integration points, typical of the cubature formulae, and the integration points are provided by ICLHS, which also taking full advantage of the sampling method. Based on this, a single-loop fractional-maximum entropy solution strategy is applied to obtain the EVD of the response. Finally, the above method is used to analyze the seismic reliability of a typical large-span single-pylon suspension bridge considering double uncertainties of ground motions and structural parameters.

The original manuscript is organized as follows, the basic theoretical methods of SRA are presented in Section 2, including the dimension reduction simulation of non-stationary ground motions, the single-loop maximum entropy method of fractional moments, along with ICLHS combaining the unequal weights, therefore a efficient framework for SRA is established in this section. Section 3 verifies the effectiveness of the proposed method via a three-story nonlinear shear frame structure calculation example compared with MCS. In the Section 4, the seismic response and SRA of a single-pylon suspension bridge are carried out based on OpenSees software, and the conclusions are presented in the last section.

2. Reliability Evaluation Of Structural Dynamic System

2.1 Reduced-dimensional simulation of stochastic ground motion

Estimating the evolutionary power spectral density function is a necessary condition to characterize the spectral characteristics of the non-stationary process of ground motion, and $X(t)$ is used to represent its random ground motion. According to Priestley's evolutionary spectrum representation theory, the non-stationary simulation of random ground motion $\hat{X}(t)$ can be expressed as [35–36]:

$$\hat{X}(t) = \sum_{k=1}^{N} \sqrt{2 S_X\left(\omega_k, t\right) \Delta\omega} \left[\cos\left(\omega_k t\right) \alpha_k + \sin\left(\omega_k t\right) \beta_k\right] \quad (1)$$

where ω_k is the discrete frequency and $\Delta\omega$ is the increment of frequency. S_X is the bilaterally evolving power spectral density function (EPSD), which is usually defined as: $S_X\left(\omega_k, t\right) = |A(\omega, t)|^2 S(\omega)$, and $A(\omega, t)$ is the random ground motion time-frequency non-smooth modulation function. The uncertainty of ground motion is characterized by the standard orthogonal random variables α_k and β_k, which satisfy the following orthogonality conditions according to the spectral representation theory [36].

$$E[\alpha_k] = E[\beta_k] = 0,\ E[\alpha_j \beta_k] = 0,\ E[\alpha_j \alpha_k] = E[\beta_j \beta_k] = \delta_{jk}$$

2

where δ_{jk} is the Kronecker-Delta function. Eq. (1) is used as an approximate expression for non-stationary random ground motion, and when N is taken to be large enough, we can obtain ground motion simulation results with a small enough error truncation; to make the truncation error small enough without losing the accuracy of the results, usually, N is taken to be in the range of 500–1000 [37]. In this case, the uncertain random variables of the most primitive ground motion are $\left\{\alpha_k, \beta_k\right\}_{k=1}^{N}$, and the dimensionality will be reduced to 2N. However, even so, the uncertainty simulation of ground motion still consists of having an ultra-high dimensional probability space. In order to improve the efficiency of non-stationary random ground motion simulation and reduce the number of random variables as well as the computational effort of structural seismic response, this investigation adopts the method of representing random variables as random functions to simulate non-stationary ground motion [36], which transforms the random variable $\left\{\alpha_k, \beta_k\right\}_{k=1}^{N}$ into an orthogonal function with only two variables, thus achieving effective dimension reduction. The orthogonal function is constructed as follows:

$$\hat{\alpha}_k = cas(k\theta_1), \hat{\beta}_k = cas(k\theta_2), k = 1, 2, \cdots, N$$

3

where $cas = \sin(\cdot) + \cos(\cdot)$ is the Hartley orthogonal basis function, $\left\{\hat{\alpha}_k, \hat{\beta}_k\right\}$ satisfies the condition shown in Eq. (2) [36].

By orthogonal function simulation, the ultra-high-dimensional random variables $\left\{\alpha_k, \beta_k\right\}$ will be reduced to 2 elementary random variables $\left\{\theta_1, \theta_2\right\}$. The process of dimension-reduced non-stationary random ground motion simulation is as follows:

(1) Generate representative sample points $\left\{\theta_1, \theta_2\right\} \in [0, 2\pi)$ of random variables that satisfy uniform distribution and are mutually independent;

(2) Substitute $\left\{\theta_1, \theta_2\right\}$ into Eq. (3) to construct the independent orthogonal random variables $\left\{\hat{\alpha}_k, \hat{\beta}_k\right\}$;

(3) Generate non-stationary ground motion by randomly mapping the random variables $\left\{\hat{\alpha}_k, \hat{\beta}_k\right\}$ into $\left\{\alpha_k, \beta_k\right\}$ Eq. (1).

2.2 Equivalent Extreme Value Theory based on EVD

Generally, the randomness of the structure under seismic ground motion is characterized by the uncertainty of the structural parameters. Assuming that $\zeta = \left\{\zeta_1, \zeta_2, \cdots, \zeta_s\right\}$ is the random variable of the structural parameters, $\theta = \left\{\theta_1, \theta_2\right\}$ denotes the random variable that determines the uncertainty of the reduced-

dimensional ground motion, then the dynamic equation of the bridge structure under seismic action can be expressed by the following equation:

$$\mathbf{M}(\zeta)\ddot{\mathbf{X}}(t) + \mathbf{C}(\zeta)\dot{\mathbf{X}}(t) + G\left[\mathbf{X}(t)\dot{\mathbf{X}}(t), \zeta\right] = -\mathbf{M}(\zeta)\mathbf{I}\ddot{x}_g(\theta, t)$$

4

where **M** is the mass matrix of the structure, **C** is the damping matrix and **G** is the non-linear restoring force vector of the structure; $\mathbf{X}(t)$, $\dot{\mathbf{X}}(t)$ and $\ddot{\mathbf{X}}(t)$ are the displacement, velocity, and acceleration vectors of the structural response, respectively, and $\ddot{x}_g(\theta, t)$ is the ground motion generated by the method described in the previous subsection. In the structural reliability analysis, the limit state functional function of the structure can be expressed as:

$$Z = H(t)$$

5

H(ζ) > 0, H(ζ) = 0, and H(ζ) < 0 correspond to the safe, limiting, and failure states, respectively. Due to the difficulty of obtaining a numerical solution, the probability of failure *R* of a structure can be transformed into a simple numerical integral according to the equivalent extreme value theory [22]:

$R = \Pr[Z_{ext}(t) \leqslant$

6

where Pr represents the probability; {Z_m} is the limit value of the limit state of the structure in performance-based earthquake engineering; {Z_{ext}} is the extreme value of the response of the structure under seismic action, and {p_{{Z_{ext}}\left(t \right)}}\left(z \right) is the EVD of the seismic response of the structure.

2.3 Maximum entropy method and single-loop solving strategy

Accurate obtaining the EVD of structures under ground motions is a critical step in SRA based on the equivalent extreme value theory. Here the maximum entropy method (MEM) proposed by E.T. Jaynes [38] is applied to obtain the probability density function of the structural extremes.

The response extremum consisting of both structural and ground shaking uncertainties is {\text{z}_{ext}}(t), denoted for convenience as *Z*. By definition, the information entropy {\rm H}(z) of a response extremum *Z* with probability density function {p_z}(z) is [38]:

{\rm H}(z)= - \int_{Z} {{p_z}(z)\log \left({{p_z}(z)} \right)dz}

7

According to the MEM, the entropy value {\rm H}(z) is maximum when obtaining the PDF of the extreme response *Z*. Eq. (7) can be equated to a nonlinear optimization problem with the constraint:

$$\left\{ {\begin{array}{*{20}{c}} {{\text{Find}}:{p_z}(z){\text{ }}} \\ {{\text{ Maximize}}}:H(z)= - \int_{Z} {{p_z}(z)\log \left({{p_z}(z)} \right)dz{\text{ }}} } \\ {s.t.\left\{ {\begin{array}{*{20}{c}} {\int_{Z} {{p_z}(z)\log \left({{p_z}(z)} \right)dz} =1} \\ {{\mu _z}^{{{\eta _r}}}=\int_{Z} {{z^{{\eta _r}}}{p_z}(z)dz} } \end{array}{\text{for }}r=1,2, \cdots ,M} \right.} \end{array}} \right. \quad (8)$$

where ${\mu _z}^{{{\eta _r}}}$ is the η_r^{th} order fractional moment of the structural extreme response and M is the truncation number of the fractional moment. Generally, the fractional moment can be expressed as follows:

$${\mu _z}^{{{\eta _r}}}=\sum\limits_{{i=1}}^{m} {{\varpi _i}z\left({{{\mathbf{\zeta }}_i},{{\mathbf{\theta }}_i}} \right)} \quad (9)$$

where ${{\mathbf{\zeta }}_i}$ and ${{\mathbf{\theta }}_i}$ are the integration points of the structural and ground motion parameters, respectively; ${\varpi _i}$ is the weight of each integration point.

By applying the Lagrange multiplier method to Eq. (7) and making the first-order partial derivative zero, the estimate of the probability density function is easily obtained as follows:

$${\hat {p}_Z}(z)=\exp \left({ - \sum\limits_{{r=0}}^{M} {{\lambda _r}{z^{{\eta _r}}}} } \right){\text{ }} \quad (10)$$

where ${\mathbf{\lambda }}={[{\lambda _0}, \cdots ,{\lambda _M}]^{\text{T}}}$ is the Lagrange multiplier; ${\eta}={[{\eta _0}, \cdots ,{\eta _M}]^{\text{T}}}$ is the fractional-order moment.

Further, to assess the difference between the estimate ${\hat {p}_Z}(z)$ and the true value ${p_Z}(z)$ of the probability density function, the evaluation is performed here by minimizing the Kullback-Leibler (K-L) divergence [39], which transforms a constrained nonlinear problem into an unconstrained optimization problem:

$$\left\{ {{\eta _r},{\lambda _r}} \right\}_{{r=1}}^{M}=\mathop {Arg}\limits_{{{\eta}{\text{\& }}{\mathbf{\lambda }}}} {\text{ min}}\left\{ {\ln \left[{\int_{Z} {\exp \left({ - \sum\limits_{{r=1}}^{M} {{\lambda _r}{z^{{\eta _r}}}} } \right)dz} } \right]+\sum\limits_{{r=0}}^{M} {{\lambda _r}{\mu _Z}^{{{\eta _r}}}} } \right\} \quad (11)$$

Due to the inclusion of a large amount of central moment information, this allows the fractional moments to fully avoid the instability caused by the integer moments in the optimization process [39]. However, the two-parameter unconstrained optimization problem remains a major challenge because the initial values of ${\mathbf{\lambda }}$ and η are generated randomly, and the optimization with double-loop results in functions that are difficult to converge, or a large number of calculations yield only local extremes. To overcome the above disadvantages, a single-loop strategy [40] will be adopted in this study to ensure the robustness of the MEM solution.

First, perform integration by parts to the constraint in Eq. (8), and then we have [41]:

$$\begin{gathered} {\mu _z}^{{{\eta _r}}}=\int_{Z} {{z^{{\eta _r}}}{p_z}(z)dz} \hfill \\ {\text{ =}}\frac{1}{{\eta r+1}}\left[{{z^{{\eta _r}+1}}{p_z}(z)} \right]_{{za}}^{{zb}}+\frac{1}{{\eta r+1}}\int_{Z} {{z^{{\eta _r}+1}}d{p_z}(z)} \hfill \\ r=0,...,M \hfill \\ \end{gathered}$$
12
where z_a and z_b are the upper and lower bounds of the response, respectively. Suppose z_a = 0 and z_b = 1 and substitute Eq. (10) into Eq. (12), such that:

$$\left({\eta _r+1} \right){\mu _z}^{{{\eta _r}}}={p_z}(1)+\sum\limits_{{k=1}}^{M} {{\lambda _k}} \,{\eta _k}\,{\mu _z}^{{({\eta _r}+{\eta _k})}}$$
13
Then, replacing i in the above equation with i + 1, Eq. (13) can be rewritten in the following form:

$$\left({\eta r+1+1} \right){\mu _z}^{{{\eta _r}+1}}={p_z}(1)+\sum\limits_{{k=1}}^{M} {{\lambda _k}} \,{\eta _k}\,{\mu _z}^{{({\eta _{r+1}}+{\eta _k})}}$$
14
Subtract Eq. (13) from Eq. (14) to obtain:

$$\left({{\eta _{r+1}}+1} \right){\mu _z}^{{{\eta _r}+1}} - \left({{\eta _r}+1} \right){\mu _z}^{{{\eta _r}}}=\sum\limits_{{k=1}}^{M} {{\lambda _k}} \,{\eta _k}\,({\mu _z}^{{({\eta _{r+1}}+{\eta _k})}} - {\mu _z}^{{({\eta _r}+{\eta _k})}})$$
15
Eventually, such a transformation makes the Lagrange multiplier {\mathbf{\lambda }}={[{\lambda _0}, \cdots ,{\lambda _M}]^{\text{T}}} linearly solvable by Eq. (15), and the original two-loop nested optimization problem of Eq. (11) is simplified to a single-loop optimization problem of Eq. (16), which effectively ensures the stability of the convergence of the optimization function with sufficient accuracy [40].

$$\left\{ {{\eta _r},{\lambda _r}} \right\}_{{r=1}}^{M}=\mathop {Arg}\limits_{{\eta}} {\text{ min}}}\left\{ {\ln \left[{\int_{Z} {\exp \left({ - \sum\limits_{{r=1}}^{M} {{\lambda _r}{\kern 1pt} {z^{{\eta _r}}}} } \right)dz} } \right]+\sum\limits_{{r=0}}^{M} {{\lambda _r}{\mu _Z}^{{{\eta _r}}} } \right\}$$
16
The above conclusion for the general case where the response extremum Z is at [z_a, z_b] can be linearly transformed by Eq. (17) to satisfy the condition.

$${{{Z}}^*}=\frac{{{{Z}} - {z_a}}}{{{z_b} - {z_a}}}$$
17

2.4 ICLHS and unequal weighted fractional moment estimation

Assuming that px(X) is the joint probability density function of the uncertain random variable X, then the fractional-order moments can be estimated by the following equation:

{\mu ^{{\eta _r}}}={\int_{{{X}}} {z{{({{X}})}^{{\eta _r}}}p} _{{X}}}({{X}})d{{X}}=\sum\limits_{{i=1}}^{m} {{\varpi _i}z{{\left({{{\bar {{{X}}}}_i}} \right)}^{{\eta _r}}},} \left({i=1,2, \cdots ,m} \right)
18
where {\bar {{{X}}}_i},i=1,2, \cdots ,m is the integration point, {\varpi _i} is the weight corresponding to the integration point. The following three aspects should be interested for the relevant sampling methods and unequal weights: (1) How to generate the set of integral points with reduced correlation? (2) How to construct the unequal positive weights of the integration points? (3) How to ensure that the number of generated integral points is sufficient? The specific steps for these three aspects of interest are as follows:

(1) For *d* random variables \bar {{{X}}}{\kern 1pt} ={\kern 1pt} \left\{ {x1,x2, \ldots ,xd} \right\}in the structure, given the number of integration point sets $M_{Rep,}$ determine the set of discrete standard positive-terminus distribution points {P_{{U}}}=\left\{ {{\mathbf{u}_q}=({u_{1,q}},{u_{2,q}}, \cdots ,{u_{d,q}}),q=1,2, \cdots ,m} \right\} by

{u_{i,q}}=\Phi _{{0,1}}^{{ - 1}}\left({\frac{{{\theta _{i,q}}}}{{m+1}}} \right)
19
where *m* is the total number of integration points, \Phi _{{0,1}}^{{ - 1}}\left(\cdot \right) is the inverse distribution of the standard normal distribution, each column of {\mathbf{\theta }}=\left\{ {{\mathbf{\theta }}_1},{\mathbf{\theta }}_2}, \cdots ,{\mathbf{\theta }}_d}} \right\} is a random permutation vector of 1,2,…,m;

(2) According to the structural random parameter distribution of interest, the sample point set is generated by

{{{P}}_{{{\tilde {{{X}}}}_i}}}=F_{i}^{{ - 1}}\left({\frac{{{{\mathbf{\theta }}_i} - {{{R}}_{{i}}}}}{m}} \right)
20
where F_i is the distribution function of the i^{th} random variable, R_i is a random vector satisfying the (0,1) uniform distribution;

(3) Estimate the covariance matrices of A and B separately, perform the Cholesky decomposition such that [30]

\left\{ {\begin{array}{*{20}{c}} {{L_0}{L_0}^{T}=\operatorname{cov} \left({{P_{{U}}}} \right)} \\ {{L_1}{L_1}^{T}=\operatorname{cov} \left({{P_{\tilde {{{X}}}}}} \right)} \end{array}} \right.
21
where L_0 and L_1 are the lower triangular matrices obtained by Cholesky decomposition, respectively. The updated set of points for local correlation stripping can be obtained by [34]

{P_{{U}}}^{*}={P_{{U}}}{\left[{{\text{inv}}({L_0})} \right]^T}{L_1}^{T}
22
where inv(•) is the matrix inverse operator. In this case, the internal arrangement of the fundamental points of {P_{{U}}}^{*} changes to {{\mathbf{\theta }}^*}_{i}\left({i=1,2, \cdots ,d} \right), the updated random

permutation matrix {{\mathbf{\theta }}^*}=\left\{ {{{\mathbf{\theta }}^*}_{1},{{\mathbf{\theta }}^*}_{2}, \cdots ,{{\mathbf{\theta }}^*}_{d}} \right\} can be obtained;

(4) Generate a new point set {\kappa _q}=({\kappa _{1,q}},{\kappa _{2,q}}, \cdots ,{\kappa _{d,q}}),q=1,2, \cdots ,m in the $[0,1]^d$ unit hypercube space based on the updated random permutation vector {{\mathbf{\theta }}^*}_{i}\left({i=1,2, \cdots ,d} \right) by

{{\kappa}_i}=\frac{{{{\mathbf{\theta }}^*}_{i} - {{{R}}_{{i}}}}}{m},i=1,2, \cdots ,d
23
(5) Repeatedly generated M_{Rep} group point sets. The uniformity of the point set was quantified using the central L2 discrepancy (CL2) [37], which was determined by

\begin{gathered} C{L_2}\left({m,P} \right)={\left({\frac{{13}}{{12}}} \right)^d} - \frac{2}{m}\sum\limits_{{i=1}}^{m} {\prod\limits_{{j=1}}^{d} {\left({1+0.5\left| {{\kappa _{j,l}} - 0.5} \right| - 0.5{{\left| {{\kappa _{j,l}} - 0.5} \right|}^2}} \right)} } \hfill \\ {\text{ +}}\frac{2}{{{m^2}}}\sum\limits_{{i=1}}^{m} {\sum\limits_{{k=1}}^{m} {\prod\limits_{{j=1}}^{d} {\left({1+0.5\left| {{\kappa _{j,l}} - 0.5} \right|+0.5\left| {{\kappa _{j,k}} - 0.5} \right| - 0.5\left| {{\kappa _{j,l}} - {\kappa _{j,k}}} \right|} \right)} } } \hfill \\ \end{gathered}
24
The smaller the CL2 discrepancy indicates that the point set is more uniform. To assess the fractional moments as accurately as possible, the point set needs to have the smallest CL2 discrepancy

\tilde {P}=\mathop {Arg}\limits_{{\left\{ {{P_1},{P_2}, \cdots ,{P_{{N_{Rep}}}}} \right\}}} {\text{ min}}\left\{ {C{L_2}\left({m,{P_1}} \right),C{L_2}\left({m,{P_2}} \right), \cdots ,C{L_2}\left({m,{P_{{N_{Rep}}}}} \right)} \right\}
25
After selecting the set of basic points, the integral points can be generated by the iso-probabilistic transformation

{{{P}}_{\tilde {{{X}}},i}}=F_{i}^{{ - 1}}\left({{{\kappa}_i}} \right)
26
(6) Using Voronoi cell elements to partition the distribution domain of the integral points generated by Eq. (26), the Voronoi cell elements are expressed as [42]

$$V_k = \left\{ \boldsymbol{y} \in ¡ \ , \mathrm{P}\boldsymbol{y} - \boldsymbol{x}_q \mathrm{P} \le \mathrm{P}\boldsymbol{y} - \boldsymbol{x}_j \mathrm{P}, \ \ j \ne q \right\} \qquad (27)$$

where {\mathbb{R}} represents the cell subdomain. For any particular point x_q, the distance from any point y in its Voronoi cell subdomain to x_q is smaller than the distance to any other particular point x_j, and satisfies

{\Omega _{{P}}}=\mathop \cup \limits_{{k=1}}^{m} {\kern 1pt} {\kern 1pt} Vk\;\quad V1 \cap V2 \cap \cdots \cap Vm=\emptyset

28
(7) The weights w_i corresponding to the integration points can be equated to the probability P_k for each Voronoi cell subdomain. The MCS numerical method is applied here to determine the probability P_k by scattering the point set {\widetilde {{{x}}}_j}=\left({{{\widetilde {x}}_{1,j}},{\widetilde {x}}_{2,j}}, \cdots , {{\widetilde {x}}_{m,j}}} \right)\quad j=1,2, \ldots ,{N_L},{N_L} \gg m in the truncated domain [23]

{w_i}={P_k} \cong \frac{\mathbb{S}}{{{N_L}}}\sum\limits_{{j=1}}^{{{N_L}}} {{f_{{X}}}\left({{{\widetilde {{{x}}}}_j}} \right)} \times I\left[{{{\widetilde {{{x}}}}_j} \in {V_k}} \right]
29
where {\mathbb{S}} represents the cubic volume. I\left[\bullet \right] is the indicator operator that satisfies

I\left[{{{\widetilde {{{x}}}}_j} \in {V_k}} \right]=\left\{ {_{{0\quad {{\widetilde {{{x}}}}_j} \notin {V_k}}}^{{1\quad {{\widetilde {{{x}}}}_j} \in {V_k}}} \right.
30
(8) Determine the number of integration points needed according to the fractional moments of the test function. Define the relative error as

e=\hbox{max} \left({\frac{{\left| {\mu _{{e - t}}^{{{\eta _r}}} - \mu _{{c - t}}^{{{\eta _r}}} \right|}}{{\left| {\mu _{{e - t}}^{{{\eta _r}}} \right|}}} \right),{\text{ }}{m_r} \in \Omega
31
where \Omega is the truncation domain of fractional order {\eta _r}, usually taken as [-3, 3]. \mu _{{e - t}}^{{{\eta _r}}} is the fractional moment obtained from the original MCS simulation, and \mu _{{c - t}}^{{{\eta _r}}} is the fractional moment estimated by the unequal-weight ICLHS method. A typical nonlinear test function is defined as [43]

Z\left({{X}} \right)=1+{{{{{X}}^T}{{X}}} \mathord{\left/ {\vphantom {{{{{X}}^T}{{X}}} 2}} \right. \kern-0pt} 2}
32
The fractional moments of the test function estimate by the crude MCS simulation are

\mu _{{e - t}}^{{{\eta _r}}}={\int_{{{X}}} {z{{({{X}})}^{{\eta _r}}}p} _{{X}}}({{X}})d{{X}}=\frac{1}{{{N_L}}}\sum\limits_{{i=1}}^{{{N_L}}} {{\left({1+{{{{\tilde {{{X}}}}_i}^{T}{{\tilde {{{X}}}}_i}} \mathord{\left/ {\vphantom {{{{\tilde {{{X}}}}_i}^{T}{{\tilde {{{X}}}}_i}} 2}} \right. \kern-0pt} 2}} \right)}^{{\eta _r}}}}
33
The fractional moments estimated by the unequally weighted ICLHS simulation are

\mu _{{c - t}}^{{{\eta _r}}}={\int_{{{X}}} {z{{({{X}})}^{{\eta _r}}}p} _{{X}}}({{X}})d{{X}}=\sum\limits_{{i=1}}^{m} {{w_i}{{\left({1+{{{{\bar {{{X}}}}_i}^{T}{{\bar {{{X}}}}_i}} \mathord{\left/ {\vphantom {{{{\bar {{{X}}}}_i}^{T}{{\bar {{{X}}}}_i}} 2}} \right. \kern-0pt} 2}} \right)}^{{\eta _r}}}}
34
For a given relative error \varepsilon, the number of integration points is considered to meet the requirement when calculating the relative error e \leqslant \varepsilon. Otherwise, the number of integration points is increased;

(9) After generating uncertain seismic waves by dimension reduction of the stochastic ground motion, perform nonlinear dynamic analysis on the structure, and finally calculate the fractional moments of the response by Eq. (18).

It should be noted that for steps (1)-(8) do not involve dynamic response analysis, which can greatly reduce the computational burden while ensuring accuracy. The complete implementation of the proposed framework for SRA of structures is shown in Fig. 1.

3. Three-story Nonlinear Shear Frame Structure Numerical Example

To verify the applicability and accuracy of the proposed framework for structural SRA, an open three-story nonlinear shear frame shown in Fig. 2 is investigated. The effectiveness of the seismic dimensionality reduction method and structural uncertainties has been verified in Ref. [34]. The story height and bay length of the frame are $h_1 = h_2 = h_3$=4m, $b_1 = b_2$ = 5m respectively, the EI of the beam is ∞, and the section size of the column is w = 400mm, h = 300mm. The nonlinear hysteretic behavior of the structure is simulated by the Bouc-Wen model [44], which has the following relevant parameters: A_B =1, α_B = 0.04, n = 1, {\delta _\gamma }= 0.02, {\delta _\eta }= 0.01, and \beta =\nu =20. The Rayleigh damping is adopted as $\mathbf{C} = \alpha\mathbf{M} + \beta\mathbf{K}$, where α = .0.2191 and β = 0.0088. The detail uncertainty parameters of the framework structure are shown in Table 1.

Table 1
The lumped mass and lateral stiffness statistics

Variable	$M_1(10^5kg)$	$M_2(10^5kg)$	$M_3(10^5kg)$	$K_1(10^7kN/m)$	$K_2(10^7kN/m)$	$K_3(10^7kN/m)$
Mean	2.71	2.71	2.71	2.42	2.42	2.42
C.O.V	0.1	0.1	0.1	0.15	0.15	0.15
Distribution	Normal	Normal	Normal	Lognormal	Lognormal	Lognormal

For the time-frequency conversion of nonstationary random ground motion, the bilateral evolutionary power spectral density (EPSD) model is used as follows [45],

S\left({\omega ,t} \right)=A{(t)^2}\frac{{{\omega _e}{{(t)}^4}+4{\omega _e}{{(t)}^2}{\xi _e}{{(t)}^2}{\omega ^2}}}{{{\left[{{\omega ^2} - {\omega _e}{{(t)}^2}} \right]}^2}+4{\omega _e}{{(t)}^2}{\xi _e}{{(t)}^2}{\omega ^2}}} \cdot \frac{{{\omega ^4}}}{{{\left[{{\omega ^2} - {\omega _f}{{(t)}^2}} \right]}^2}+4{\omega _f}{{(t)}^2}{\xi _f}{{(t)}^2}{\omega ^2}}} \cdot {S_0}(t)
35
where {S_0}(t) is the seismic intensity factor, A(t) is the time modulation function. Futherly,

{S_0}(t)=\frac{{\bar {a}_{{\hbox{max} }}^{2}}}{{{{\bar {\gamma }}^2}\left[{\pi {\omega _e}(t)\left({2{\xi _e}(t)} \right)+\frac{1}{{2{\xi _e}(t)}} \right]}}

36

A(t)={\left[{\frac{t}{c}\exp \left({1 - \frac{t}{c}} \right)} \right]^d}

37

{\omega _e}(t)={\omega _0} - a\frac{t}{T},{\xi _e}(t)={\xi _0}+b\frac{t}{T},{\omega _f}(t)=0.1{\omega _e}(t), {\xi _f}(t)={\xi _e}(t)

38

where T is the duration of ground motion. \bar {a}_{{\hbox{max} }}^{{}} is the peak acceleration of ground motion. {\omega _0}, {\xi _0}, a and b are site conditions and design seismic characteristic parameters. In this investigation, The parameters of the EPSD are set as: T = 20.96s, a = 3, b = 0.35, c = 6, d = 2, and \bar {\gamma }=2.75. The peak acceleration value of ground motion is taken as {\bar {a}_{max}}=196{{cm} \mathord{\left/ {\vphantom {{cm} {{s^2}}}} \right. \kern-0pt} {{s^2}}}. Via the dimensionality reduction simulation of ground motion, the high-dimensional random variables can be reduced to only two basic random variables. Two generated representative ground motion samples and the seismic inter-story drift response of the first floor are shown in Fig. 3, as well as the non-stationary frequency characteristics of ground motions and the nonlinearity seismic behaviour of structure can be observed from Fig. 3.

The fractional moment of structural response is evaluated by the ICLHS combining unequal weights proposed in this paper. Before dynamic time-history analysis, 200, 300, and 400 sample points are generated respectively. The partition distribution domain of sample points is gotten using the Voronoi cell, and the weights of the distribution domain can be calculated by MCS. The voronoi cells in the two-dimensional distribution domain are shown in Fig. 4. According to the test function, the relative errors of fractional moment between the ICLHS combining unequal weight and the crude MCS (10^6 times) is calculated in the truncated domain [-2, 3], which was shown in Fig. 5, the maximum relative error is 3.38%, 2.73%, and 2.33% via 200,300 and 400 sample points, respectively. For the tolerance error taken as ε = 3%, the accuracy of fractional moment calculation in the truncated domain of interest is acceptable when m = 300. Therefore, the total number of samples can be determined as M = 300.

Based on the 300 sample points and nonstationary ground motions generated by the above method, 300 deterministic nonlinear structural dynamic analyses are performed on the structure. The fractional moments of inter-story drift response of the first floor are evaluated by Eq. 18, and the simple search of the unconstrained optimization function Eq. 16 is performed according to the single-loop solution strategy to obtain the fractional-order η = [-0.3413, 1.7462, -0.5787] and the Lagrange multiplier λ = [-1.6314, 2.935e-05, 0.0486], which satisfy the maximum condition. It is worth mentioning that the optimal solution is obtained after only 178 iterations of search by the single-loop strategy solution, which greatly improves the efficiency and stability of the objective function optimization .

Further, the EVD of response extreme value {z_{ext}}(t) can be obtained by substituting the optimized fractional-order and Lagrange multiplier into Eq. 10 as initial conditions, as shown in Fig. 6 (a). It is well known that the accuracy of MCS is based on a huge time-consuming, which is unrealistic when simulating

complex nonlinear structures. As a comparison, Fig. 6(a) also plots the EVD histogram for crude MCS (10^5 times) and the probability density curve for kernel density estimation. The results show that the fractional-order moments calculated by the unequal weights combining ICLHS method are consistent with the crude MCS calculation, especially in the tail of the PDF, which can present the information contained in the fractional moments completely. In Fig. 6(b), the CDF curves of the proposed method and crude MCS are plotted according to the response extremes, from which a good fitting between the two curves can be observed.

Table 2
Comparisons of failure probabilities

Limit-value (m)	**0.040**	**0.045**	**0.050**	**0.055**	**0.060**
Proposed method	0.05986	0.02740	0.01203	0.00459	0.00088
MCS	0.06043	0.02687	0.01157	0.00428	0.00071

After successfully estimating the EVD of the structure, the failure probability of the structure can be obtained from a simple numerical integration. For the cases where the inter-story drift limits are taken differently, Table 2 gives the failure probabilities obtained by the proposed method and crude MCS, and the results are well matched, which indicates that the proposed method is sufficiently accurate for structural dynamic systems, especially for low probability failure systems (P_f<10^{-3}). It is worth mentioning that only 300 nonlinear dynamic analyses are performed, and the computational effort is only 3/1000 of that of the MCS method, which proves the excellent efficiency of the proposed method.

4. Sesimic Reliability Of The Single-pylon Suspension Bridge

4.1 Engineering background

In this study, an asymmetric large-span and single-pylon suspension bridge with a main span of 780m in Yunnan Province is employed to study the seismic reliability of complex nonlinear structures. The used suspension bridge has the rise-span ratio 1/11 of main cable and owns streamlined flat steel box girder with width of 31.4 m. The main tower near Yuxi shore with height of 156 m adopts reinforced concrete portal frame structure whose column body is rectangular hollow box section. In addition the rectangular hollow box section is utilized in cross beam of main tower. The group pile foundation laid under main tower is adopted to ensure adequate stability and strength of foundation. The pile cap with thickness of 7 m and dimension of 21.6 m × 21.6 m connects firmly sixteen cast-in-place piles arranged by 4 m × 4 m with diameter of 2.5 m. Among them, the layout of the suspension bridge is shown in Fig. 7.

4.2 Finite element modeling

Based on the OpenSees platform, a three-dimensional nonlinear finite element model was built as shown in Fig. 8. In which, a Elastic beam-column element is used to model the main girder of the suspension bridge. As the main vulnerable component of suspension bridge under ground mitons, the nonlinear beam-column element and fiber section are used to simulate the nonlinear seismic behavior of pylon. Also, the

Concrete02 and Kent-Scott-Park constitutive models in OpenSees are used to simulate the confined concrete in the core and the unconstrained concrete with nonlinear reactions, respectively [46]. The reinforcement bar is defined by Steel02, using the Giuffre-Menegoto-Pinto constitutive model [47]. Since suspension bridges are characterized by large spans and flexibility, the nonlinear effects of the main cables and suspenders (including prestressing effects and stress stiffening effects) are particularly obvious, which are simulated here using the Truss element. The vertical compressive load capacity of the bearing is simulated by Zero-Length Element and Harding Materials. Since the soil-pile interaction (SPI) cannot be neglected in the seismic action analysis of large-span suspension bridges, the SPI is simulated by the *p-y* method in this study, and the *p-y* nonlinear behavior is simulated by Zero-Length Element in the finite element model. Table 3 summarizes the materials and elements used for the finite element modeling of each component of the suspension bridge.

Table 3
Summary of materials and elements used in OpenSees

Component	Materials	Element
Girder	Concrete02	Elastic beam-column
Pylon	Concrete02 Steel02	Non-linear beam-column
Cable	Harding Materials Initial strain Material	Truss
Suspender	Harding Materials Initial strain Material	Truss
Bearing	Hardening	Two-node link
Pile	Concrete02 Steel02	Non-linear beam-column

4.3 Ground Motions

In this investigation, the suspension bridge is located in the strong earthquake zone in the western mountainous area of China, the seismic peak acceleration is taken as \bar {a}_{{\hbox{max}}}^{{}}=392{{cm} \mathord{\left/ {\vphantom {{cm} {{s^2}}}} \right. \kern-0pt} {{s^2}}}. The non-stationary random ground motion is generated using a bilateral evolutionary power spectral density (EPSD) model, the EPSD function is as follows [45]

$$S\left({\omega ,t} \right)=A{(t)^2}\frac{{{\omega _e}{{(t)}^4}+4{\omega _e}{{(t)}^2}{\xi _e}{{(t)}^2}{\omega ^2}}}{{{\left[{{\omega ^2} - {\omega _e}{{(t)}^2}} \right]}^2}+4{\omega _e}{{(t)}^2}{\xi _e}{{(t)}^2}{\omega ^2}}} \cdot \frac{{{\omega ^4}}}{{{\left[{{\omega ^2} - {\omega _f}{{(t)}^2}} \right]}^2}+4{\omega _f}{{(t)}^2}{\xi _f}{{(t)}^2}{\omega ^2}}} \cdot {S_0}(t)$$

39

Where {S_0}(t) is the seismic intensity factor, A(t) is the time modulation function. The values are as follows

{S_0}(t)=\frac{{\bar {a}_{{\hbox{max} }}^{2}}}{{{\bar {\gamma }}^2}\left[{\pi {\omega _e}(t)\left({2{\xi _e}(t)} \right)+\frac{1}{{2{\xi _e}(t)}} \right]}}
40
A(t)={\left[{\frac{t}{c}\exp \left({1 - \frac{t}{c}} \right)} \right]^d}
41
{\omega _e}(t)={\omega _0} - a\frac{t}{T},{\xi _e}(t)={\xi _0}+b\frac{t}{T},{\omega _f}(t)=0.1{\omega _e}(t), {\xi _f}(t)={\xi _e}(t)
42
In which, T is the duration of ground motion. {\omega _0}, {\xi _0}, a and b are the site conditions and design seismic characteristic parameters. In the present example, the parameters of the EPSD are taken as T = 40.96s, a = 3, b = 0.35, c = 6, d = 2, and \bar {\gamma }=2.75. To represent the uncertainty of ground motion, the high-dimensional random variables of ground motion can be effectively reduced to 2 basic random variables by orthogonal stochastic functions according to the ground motion reduced dimensional simulation method in the proposed framework. Two samples of non-stationary ground motion and the moment-curvature hysteresis curves of the pylon bottom section are shown in Fig. 9 and Fig. 10, respectively, and the non-stationary characteristics of ground motion and the non-linearity seismic performation of the structure can be observed in the Fig. 9 and Fig. 10.

4.4 Seismic Reliability Analysis of Suspension Bridge

To evaluate the SRA of the suspension bridge under seismic ground motions, the critical cross sections 1–1 to 5–5 of the bridge pylon, which as shown in Fig. 11, and the bearings were selected as the vulnerable componets of bidge according to the deformation failure criterion. The curvature values of the cross section in the longitudinal and transverse direction at the different limit states were determined from the equivalent curves of the section moment-curvature curves, as shown in Fig. 12, and the detail data can be found in Table 4.

The pylon, as the main vunlnerable component of the suspension bridge, the overall structure will lose the stability once it fails, so the longitudinal reinforcement yielding of the pylon bottom section is defined as pylon failure [48]. The performance index of the bearing as the connecting member between the girder and the pylon can be expressed by the relative displacement, and the ultimate displacement of 250mm is taken as the failure index of the bearing [49].

Table 4
Curvature failure index of the pylon sections in longitudinal and transverse (in brackets) direction

State	First yield of longitudinal reinforcement (1E-04)	Section equivalent yield (1E-04)	Maximum bending moment of section (1E-04)	Ultimate strain of concrete (1E-03)
Sec1-1	2.58 (2.92)	3.22 (1.80)	7.77 (8.78)	1.61 (1.82)
Sec2-2	2.92 (3.43)	3.72 (4.28)	9.08 (10.72)	1.86 (2.17)
Sec3-3	3.00 (3.52)	3.80 (4.36)	9.30 (10.96)	1.89 (2.21)
Sec4-4	3.52 (4.12)	4.31 (5.02)	10.48 (12.28)	2.16 (2.53)
Sec5-5	3.68 (4.32)	4.45 (5.19)	10.98 (12.88)	2.26 (2.65)

To characterize the uncertainty of the structural parameters, 9 major parameters were selected concerning the uncertainty parameters considered in previous bridge studies, and the distribution characteristics of the parameters are summarized in Table 5. Thus, the nonlinear dynamic system of this suspension bridge structure contains a total of 11 random variables. Similar to the previous example, when the total number of samples m = 400, the maximum relative error of the fractional moments of the test function in the potential domain is 2.94%, which satisfies the error requirement, therefore total 400 integration points are selected to evaluate the fractional moments of the seismic response of the suspension bridge.

Table 5
Uncertainty parameters of the bridge considered in the model

Component	Variable	Description	Distribution	Mean-value	COV
Pylon	Ec1	Young's modulus of concrete	Normal	3.25E + 10	0.08
	Fc	Peak intensity	Normal	2.68E + 07	0.135
	Pc	Peak strain	Normal	0.002	0.1
	Fcu	Ultimate compressive stress	Normal	5.30E + 06	0.135
	Pcu	Ultimate compressive strain	Normal	0.01	0.1
	Fy	yield strength of steel	Normal	3.35E + 08	0.04
Cable	Fy2	yield strength of cable	Normal	1.86E + 09	0.05
	Ec2	Young's modulus of cable	Normal	1.95E + 11	0.1
Pile	Ec3	Young's modulus of concrete	Normal	3.00E + 10	0.08

After performing 400 nonlinear dynamic analyses, the maximum curvature of pylon at section 1–1 are 3.74E-4 and 1.13E-4 in longitudinal and transverse direction, respectively, and the maximum longitudinal curvature exceeds the failure index of section equivalent yield, which means the section yield and plastic hinge occur in the longitudinal direction. The curvature response of sections 1–1 under representative ground motion in longitudinal and transverse direction are shown in Fig. 12. The pylon central section 2–2 is located at the lower side of the pylon central beam and has a large stress concentration because it shares the main beam load with the pylon beam, its longitudinal and transverse maximum curvature is 3.81E-4 and 1.20E-4 respectively, and the longitudinal maximum curvature exceeds the curvature failure index, and its response curve is shown in Fig. 13. The central section 3–3 of the pylon is located on the upper side of the pylon beam, and the maximum longitudinal curvature is 3.05E-04, which is slightly greater than the failure indicator, while the maximum transverse curvature is 7.80E-5, which is within the safe range. Section 4–4 and Section 5–5 are located on the upper and lower sides of the top beam of the pylon, respectively. the maximum curvature of Section 4–4 in longitudinal and transverse directions is 5.25E-05, which does not exceed the failure index of 3.68E-04. the maximum curvature of Section 5–5 is 5.0E-05, which is still less than the failure limit. Due to the variable section arrangement, the damage failure of the bridge pylon may occur in the longitudinal section of the middle and lower sections part of the pylon. Figure 14 shows the response curve of the bearing under the representative ground motion. As a replaceable member, the bearing is normally in the failure state under the strong earthquake in order to dissipate energy. Under 0.4g ground shaking, its maximum relative displacement is 0.73m, which is far beyond the failure index.

Further, the fractional moments are solved according to the extremes of the structural response and the EVD of the response is obtained by the single-loop maximum entropy method. Finally, the failure probability of the bridge componets is obtained by simply integrating the EVD numerically. The longitudinal PDF and CDF curves of sections 1–1, 2–2, and 3–3 are shown in Fig. 15. From Fig. 15(a), it can be seen that the extreme responses of sections 1–1 and 2–2 are very close to each other, and, logically, this phenomenon occurs in the lower sections of pylon where the stiffness of the bridge pylon changes gently. The failure probabilities of the sections are marked in Fig. 15(b) according to the failure index, which is 0.6398, 0.3334, and 0.0008, respectively, which indicate that section 1–1 and section 2–2 have the possibility of simultaneous failure to make the bridge pylon lose its load-carrying capacity. Figure 16 shows the PDF and CDF of transverse sections 1–3. Compared with the longitudinal sections, the response extremes of the transverse sections are small and none of them reach the failure limit. Sections 4–4 and 5–5 are located on the upper and lower sides of the crossbeam at the top of the pylon, which mainly bear the vertical concentrated forces of the suspension cables and have good stability during the earthquake. The extreme values of curvature of their longitudinal and transverse sections are small, and none of them exceeds the failure index, and the probability distribution curves of the sections are plotted in Fig. 17. The distribution information of the main beam bearing response is shown in Fig. 18. It can be noted from the figure that the relative displacement of the bearing under 0.4g earthquake far exceeds the damage limit of 0.25, which belongs to the component of complete failure.

Through the above analysis, it can be seen that the bearing of the suspension bridge, as the first line of defense, is the first to fail. As an important load-bearing member, the failure of the pylon mainly occurs in the longitudinal direction of the section 1–1 and 2–2, which is a relatively weak part. In the seismic fortification arrangement of the suspension bridge, attention should be paid to the bottom and middle section of the pylon in the transverse direction, the perfect anti-seismic measures should be utilized. Because the layout of the transverse section of the bridge tower is conservative, its response is much smaller than the longitudinal section, and the failure index is not exceeded.

5. Conclusions

This paper presents a framework for SRA of complex nonlinear structures including dimension reduction simulation of nonstationary ground motions, single-loop maximum entropy theory of fractional moments, along with improved correlation-reduced Latin hypercube sampling method (ICLHS). Therefore, a novel method for obtaining fractional moments via unequal weights combining ICLHS is proposed in this investigation, The applicability of the proposed method is verified by a three-story nonlinear shear frame, and the SRA of actual railway large-span single-pylon suspension bridge is carried out. The conclusions are as follows:

(1) The proposed method of obtaining fractional moments via unequal weights combining ICLHS takes into account the advantages of the relevant sampling method and cubature formulae, which has better applicability and accuracy. Compared with the crude MCS, this method can accurately construct the certain distribution and tail information of EVD with a lower sampling number, which verified by a verified by a three-story nonlinear shear frame.

(2) The double uncertainties of seismic ground motions and structural parameters has a small effect on the EVD main body, but for bridge structural reliability analysis, it will increase the failure probability and make it closer to the real value. The effect of this double uncertainty cannot be neglected in the SRA of complex nonlinear structures.

(3) SRA of the suspension bridge considering double uncertainty shows that the failure of the bridge pylon may occur in its longitudinal sections and the arrangement of transverse sections is on the conservative side. Via 400 deterministic dynamic response analyses, the curvature of the bridge pylon exceeded the failure index only in the longitudinal direction for sections 1–1, 2–2, and 3–3, with probabilities of failure of 0.6398, 0.3334, and 0.0008, respectively. The displacement extremes of the bearings all exceeded the failure index which belongs to the complete failure state.

(4) The main objective of this study is to establish a framework for seismic reliability assessment of bridges, the application of advanced theoretical methods to the SRA of suspension bridges was investigated, which could be applied to actual nonlinear complex structures. Therefore, the combination of the reliability of components to the system reliability is not considered in the analysis process. The reliability analysis of bridge system considering the combination of components needs to be further studied.

Declarations

ACKNOWLEDGMENTS

The research reported in this paper was supported by National Natural Science Foundation of China (No.52008047), Postdoctoral Science Foundation of China (No.2020M673294), State Key Laboratory of Geohazard Prevention and Geoenvironment Protection Independent Research Project (No.SKLGP2018Z008) and Sichuan Science and Technology Program (No. 2020YJ0081). Their supports are gratefully acknowledged.

References

1. Zanini M A , Faleschini F , Pellegrino C . Probabilistic seismic risk forecasting of aging bridge networks [J]. Engineering Structures, 2017, 136(APR.1):219-232.
2. Chen JB, Lin P-H, Li J. Pdem-based response analysis of nonlinear systems with double uncertainties. In: Multiscale modeling and uncertainty quantification of materials and structures, Springer; 2014, p. 247–56.
3. Xu J, Feng D C. Seismic response analysis of nonlinear structures with uncertain parameters under stochastic ground motions. Soil DynEarthqEng 2018; 111: 149-159.
4. Lin JH, Shen WP, Williams FW. Accurate high-speed computation of nonstationary random structural response. Eng Struct, 1997,19:586–93.
5. Lin JH, Zhao Y, Zhang Y. Accurate and highly efficient algorithms for structural stationary/ non-stationary random responses. Comput Methods Appl Mech Eng, 2001;191:103–11.
6. Wen Y K. Equivalent linearization for hysteretic systems under random excitation. Journal of Applied Mechanics 1980; 47(1): 150-154.
7. Fujimura K, Der Kiureghian A. Tail-equivalent linearization method for nonlinear random vibration. ProbabEng Mech 2007; 22(1): 63-76.
8. Chen JB, Yuan S. Dimension reduction of the FPK equation via an equivalence of probability flux for additively excited systems. J Eng Mech 2014;140(11):04014088.
9. Li J, Chen JB. Stochastic dynamics of structures. Singapore: Wiley; 2009.
10. Li J, Chen J. Probability density evolution method for dynamic response analysis of structures with uncertain parameters. Comput Mech 2004;34(5):400–9.
11. Kleiber M, Hien TD. The stochastic finite element method: basic perturbation technique and computer implementation. Wiley; 1992.
12. Xiu D, Hesthaven JS. High-order collocation methods for differential equations with random inputs. SIAM J Sci Comput 2005;27(3):1118–39.
13. Xiu D. Fast numerical methods for stochastic computations: a review. CommunComput Phys 2009;5(2–4):242–72.

14. Kougioumtzoglou IA, Spanos PD. An analytical wiener path integral technique for non-stationary response determination of nonlinear oscillators. ProbabEng Mech 2012;28(4):125–31.
15. Matteo AD, Kougioumtzoglou IA, Pirrotta A, Spanos PD, Paola MD. Stochastic response determination of nonlinear oscillators with fractional derivatives elements via the wiener path integral. ProbabEng Mech 2014;38:127–35.
16. Zhang J, Bi K, Zheng S, et al. Seismic system reliability analysis of bridges using the multiplicative dimensional reduction method. Struct Infrastruct E 2018; 14(11): 1455-1469.
17. Shinozuka M. Monte carlo solution of structural dynamics. Comput Struct 1972; 2: 855–74.
18. AU S K, BECK J L. Estimation of small failure probabilities in high dimensions by subset simulation. ProbabEng Mech 2001; 16(4): 263-277.
19. Schuller GI. Developments in stochastic structural mechanics. Arch Appl Mech 2006; 75(10):755–73.
20. Echard B, Gayton N, Lemaire M. AK-MCS: an active learning reliability method combining Kriging and Monte Carlo simulation. Struct Saf 2011; 33(2): 145-154.
21. Chen J-B, Li J. The extreme value distribution and dynamic reliability analysisof nonlinear structures with uncertain parameters. Struct Saf 2007;29 (2):77–93.
22. Li J, Chen J, Fan W. The equivalent extreme-value event and evaluation of the structural system reliability. Struct Saf 2007; 29(2): 112-131.
23. Xu J, Zhang W, Sun R. Efficient reliability assessment of structural dynamic systems with unequal weighted quasi-Monte Carlo Simulation. Comput Struct 2016; 175: 37-51
24. Hua L-K, Wang Y. Applications of number theory to numerical analysis. Springer Science & Business Media; 2012.
25. Halton JH. On the efficiency of certain quasi-random sequences of points in evaluating multi-dimensional integrals. Numer Math 1960;2(1):84–90.
26. Sobel IM. On quasi-Monte Carlo integrations. Math Comput Simul 1998;47 (2):103–12.
27. Gerstner T, Griebel M. Numerical integration using sparse grids. Numer Algor 1998;18(3–4):209–32.
28. Smolyak SA. Quadrature and interpolation formulas for tensor products of certain classes of functions. DoklAkadNauk SSSR 1963;4:123.
29. Shields M D, Zhang J. The generalization of Latin hypercube sampling[J]. Reliability Engineering & System Safety, 2016,148: 96-108.
30. OLSSON A M J, Sandberg G E. Latin hypercube sampling for stochastic finite element analysis. J Eng Mech 2002; 128(1):121-125.
31. Castaldo, P., Gino, D., Mancini, G. Safety formats for non-linear finite element analysis of reinforced concrete structures: discussion, comparison and proposals[J]. Engineering Structures, 2019, 193: 136-153.
32. Castaldo, P., Mancini, G., Palazzo, B. Seismic reliability-based robustness assessment of three-dimensional reinforced concrete systems equipped with single-concave sliding devices[J]. Engineering Structures, 2018, 163:373-387.

33. Zhang J, Chen K J, Zeng Y P, et al. Seismic Reliability analysis of Cable-Stayed Bridges Subjected to Spatially Varying Ground Motions[J]. International Journal of Structural Stability and Dynamics, 2021:2150094.
34. Chen Z Q, Zheng S X, Zhang J, et al. Seismic reliability analysis of high-pier railway bridges with correlated random parameters via an improved maximum entropy method[J]. Structures, 2021, 33(October 2021):4538-4555.
35. Xu J, Feng D C. Stochastic dynamic response analysis andreliability assessment of non-linear structures under fullynon-stationary ground motions[J]. Structural Safety, 2019, 79:94-106.
36. Liu Z, Liu W, Peng Y. Random function based spectralrepresentation of stationary and non-stationary stochasticprocesses[J]. Probabilistic Engineering Mechanics, 2016, 45:115-126.
37. Xu J, Feng DC. Seismic response analysis of nonlinear structures with uncertain parameters under stochastic ground motions. Soil DynEarthqEng, 2018,111:149-159.
38. Jaynes ET. Information theory and statistical mechanics. Phys Rev 1957;106(4):620.
39. Zhang X, Pandey M D. Structural reliability analysis based on the concepts of entropy, fractional moment and dimensional reduction method. Struct Saf 2013; 43: 28-40.
40. Li G , He W , Zeng Y . An improved maximum entropy method via fractional moments with Laplace transform for reliability analysis[J]. Structural and Multidisciplinary Optimization, 2018, 59.
41. Erdogmus D, Hild KE, Rao YN, Principe JC (2004) Minimax mutualinformation approach for independent component analysis. NeuralComput 16(6):1235–1252
42. Chen J B , Ghanem R , Jie L . Partition of the probability-assigned space in probability density evolution analysis of nonlinear stochastic structures[J]. Probabilistic Engineering Mechanics, 2009, 24(1):27-42.
43. Xu H, Rahman S. A generalized dimension-reduction method formultidimensional integration in stochastic mechanics. Int J Numer MethodsEng 2004;61(12):1992–2019.
44. Xu J, Dang C, Kong F. Efficient reliability analysis of structures with the rotational quasi-symmetricpoint-and the maximum entropy methods. Mech Syst Signal Process 2017; 95: 58-76.
45. Cacciola P, Deodatis G. A method for generating fully non-stationery and spectrum-compatible groundmotion vector processes. Soil DynEarthqEng 2011; 31(3): 351-360.
46. C. Kent, R. Park, Flexural members with confined concrete, J. Struct. Div. 97 (07) (1971) 1969–1990.
47. Menegotto, Method of analysis for cyclically loaded RC plane frames including changes in geometry and non-elastic behavior of elements under combinednormal force and bending, Resistance and Ultimate Deformability of Structures Acted on by Well Defined Repeated Loads, IABSE, Lisbon, 1973: 15-2.
48. Zong Z H, Huang X Y, Li Y L, et al. Study of Collapse Failure and Failure Control of Long Span Cable-Stayed Bridges Under Strong Earthquake Excitation [J]. Bridge Construction, 2016(1):24-29.(In Chinese)
49. Nielson BG, Analytical Fragility Curves for Highway Bridges in Moderate Seismic Zones [J].Georgia institute of Technology, 2005

Figures

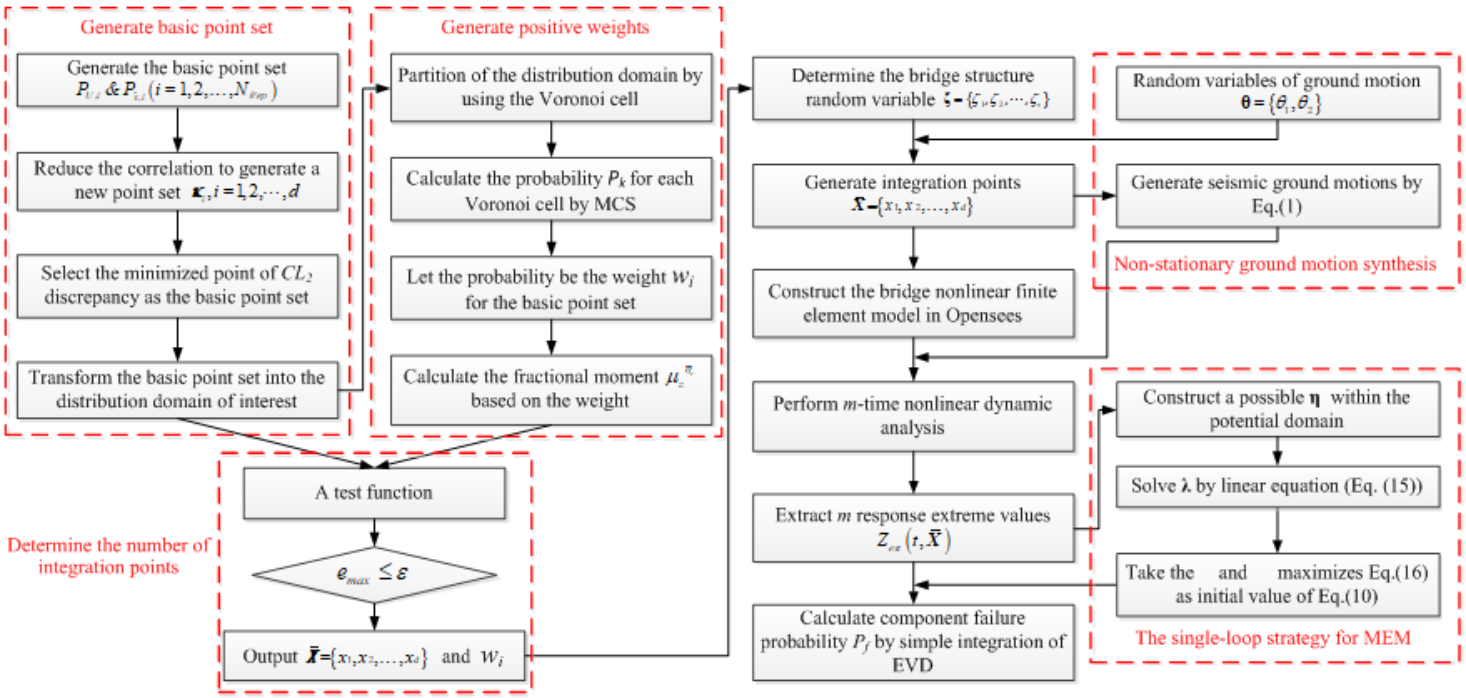

Figure 1

Implementation flowchart of the proposed method

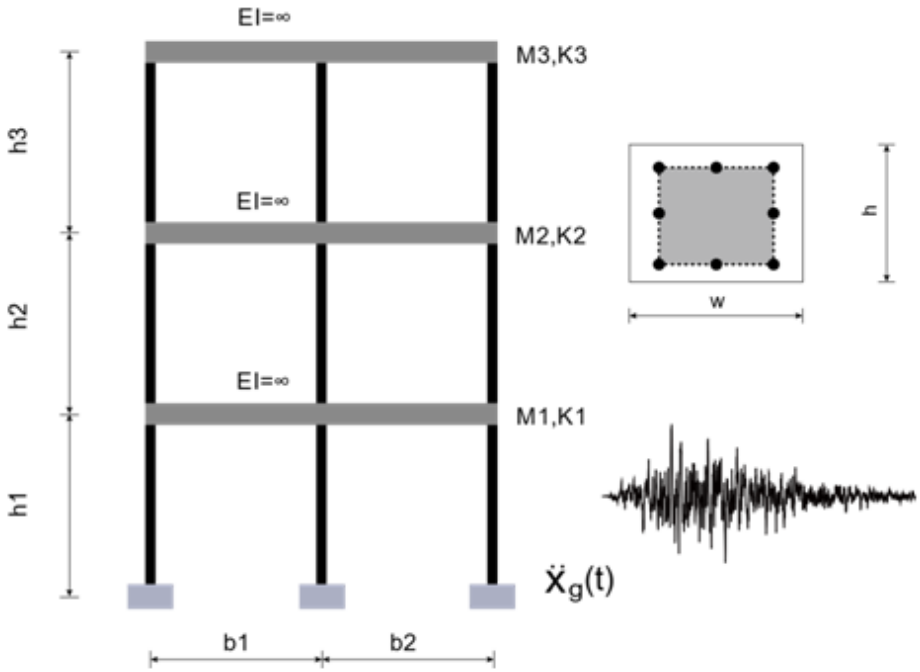

Figure 2

The three-story nonlinear frame structure

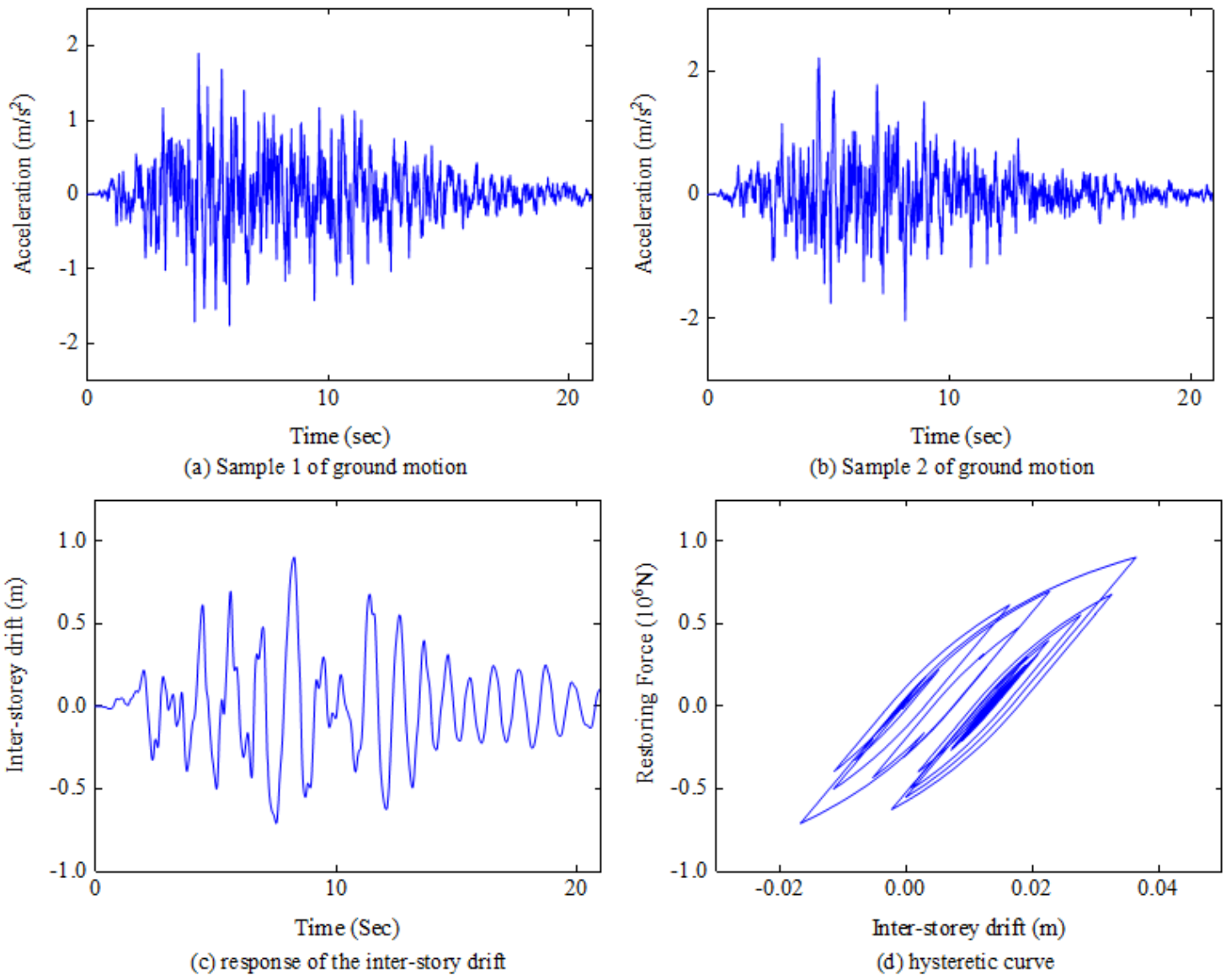

Figure 3

Nonstationary random ground motion samples and structuralseismic response

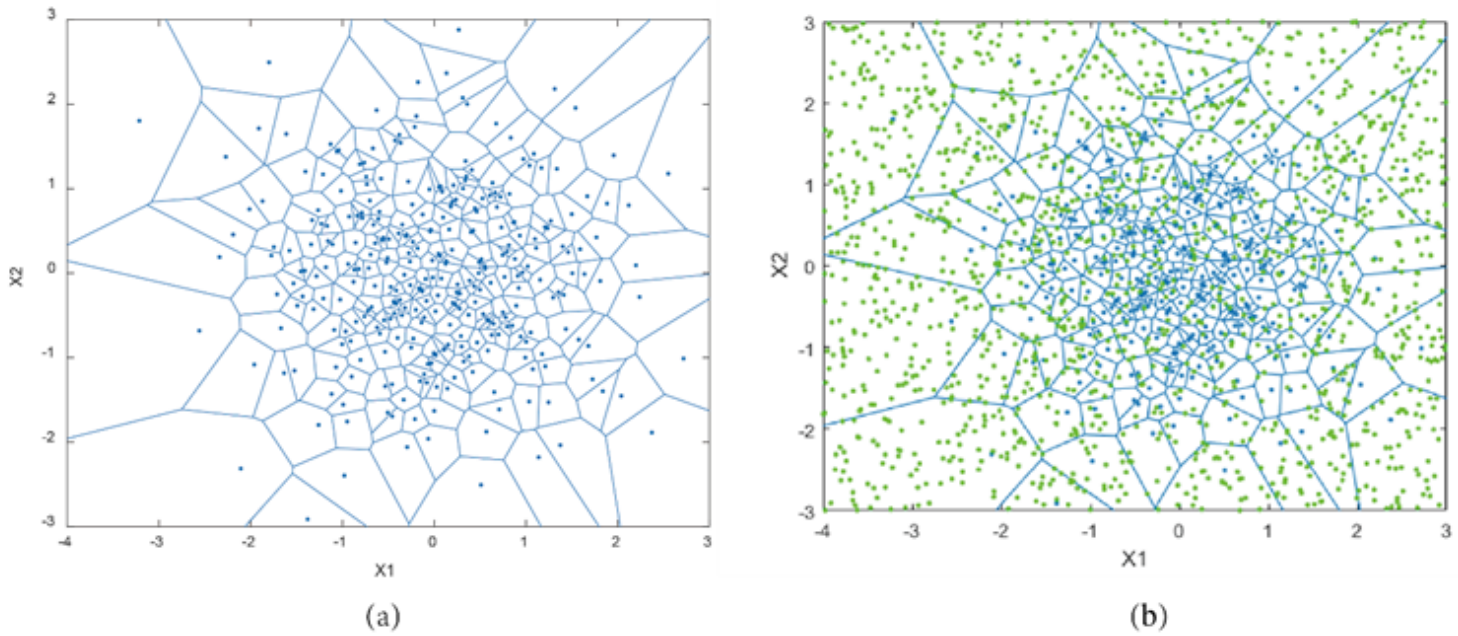

Figure 4

Voronoi cells(a) Two-dimension (b) Monte Carlo Simulation.

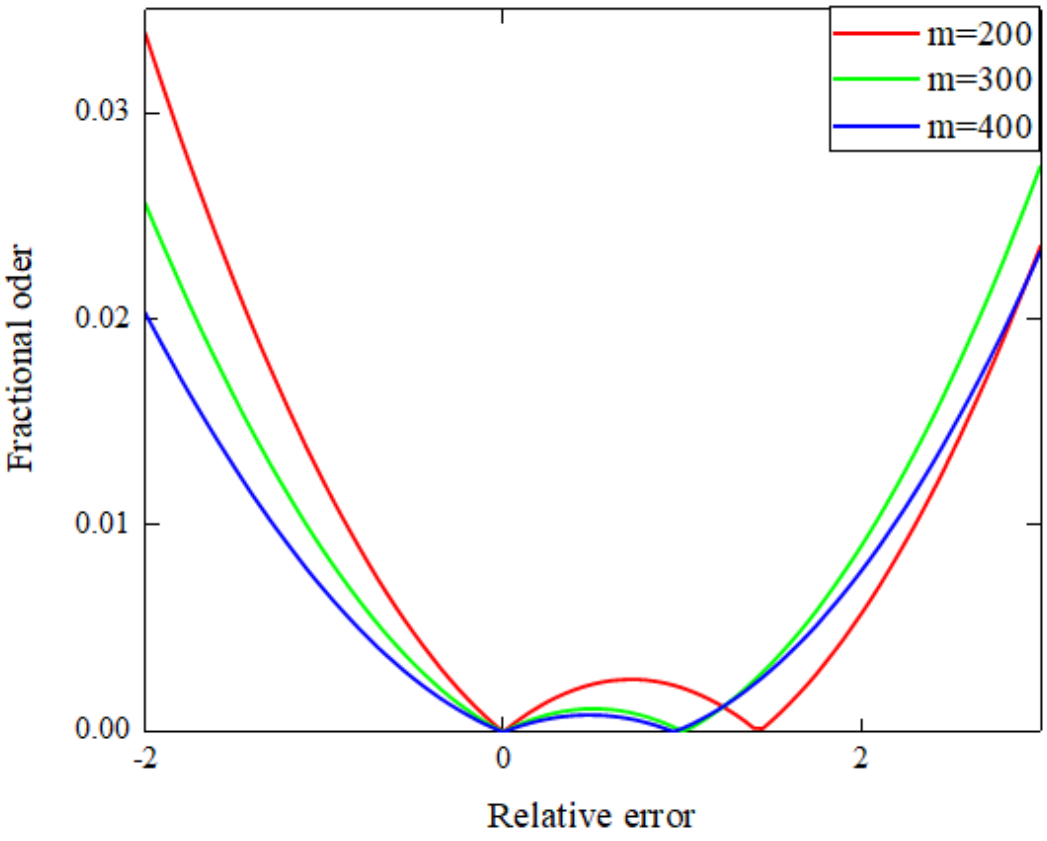

Figure 5

Test function relative error v.s. fractional moment.

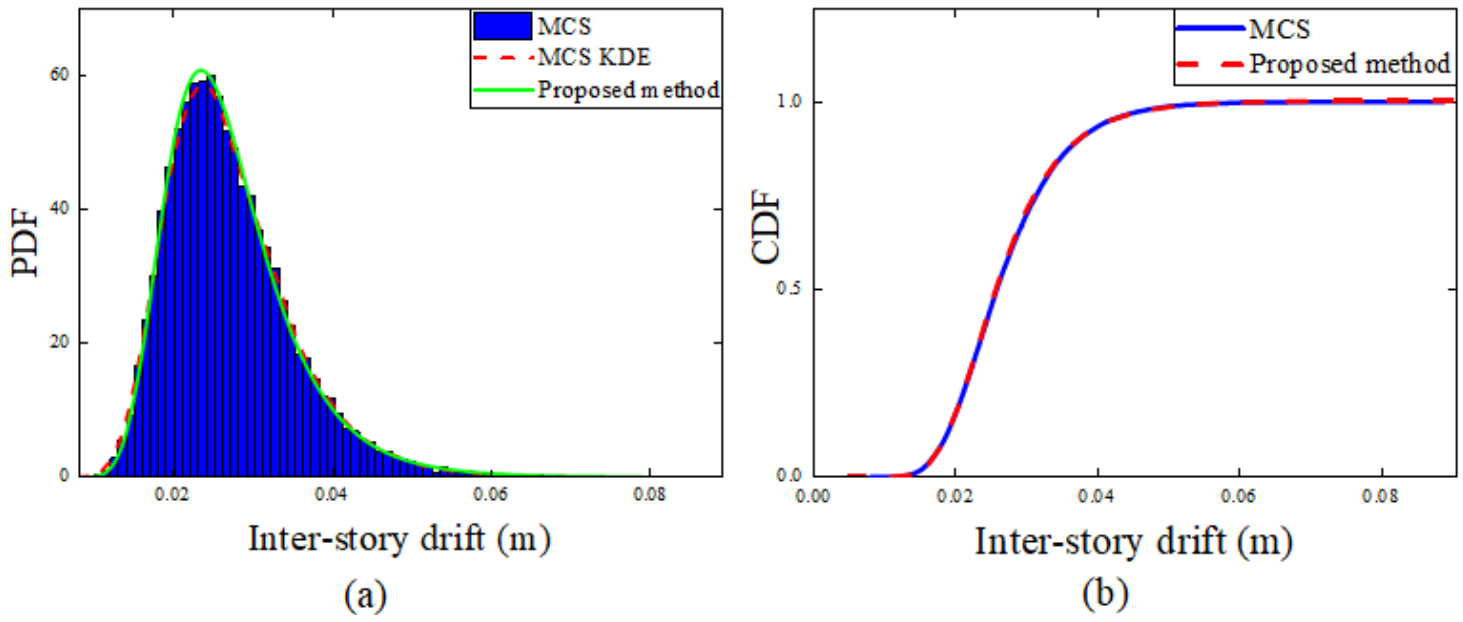

Figure 6

EVD evaluation (0-1 inter-story drift).

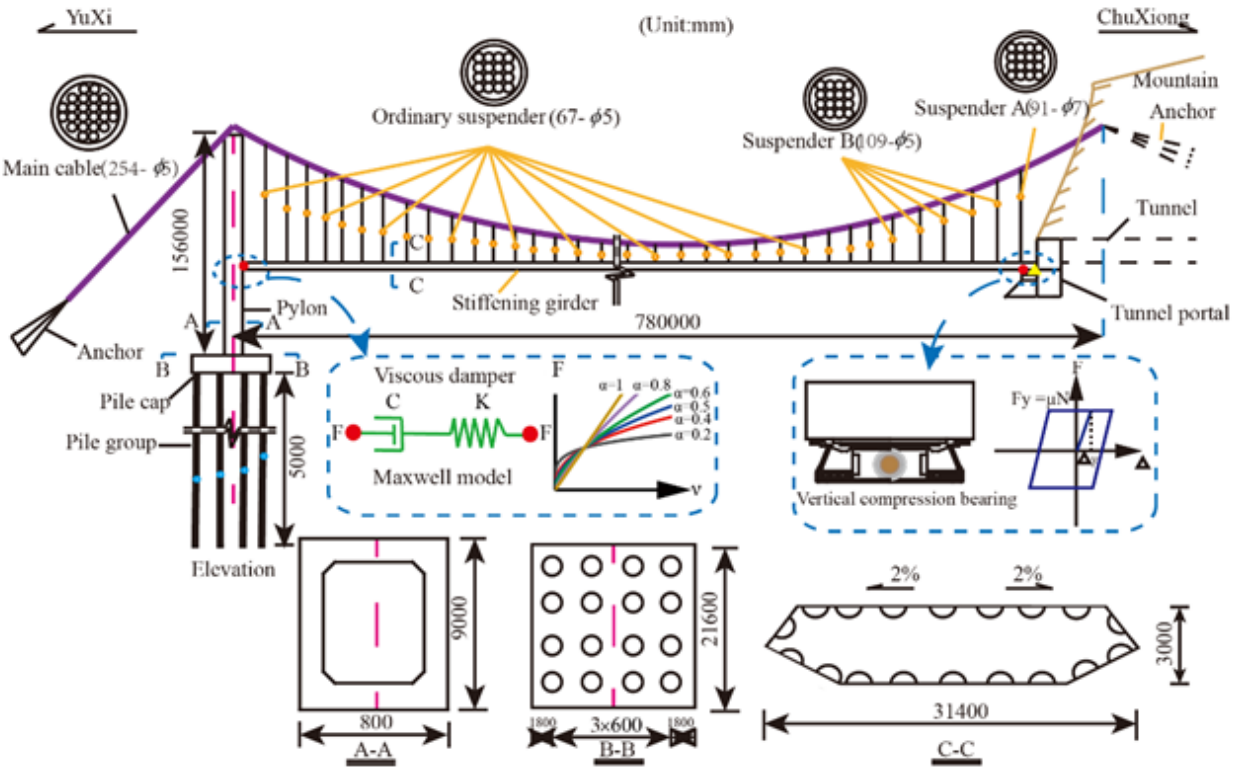

Figure 7

Layout plan of suspension bridge

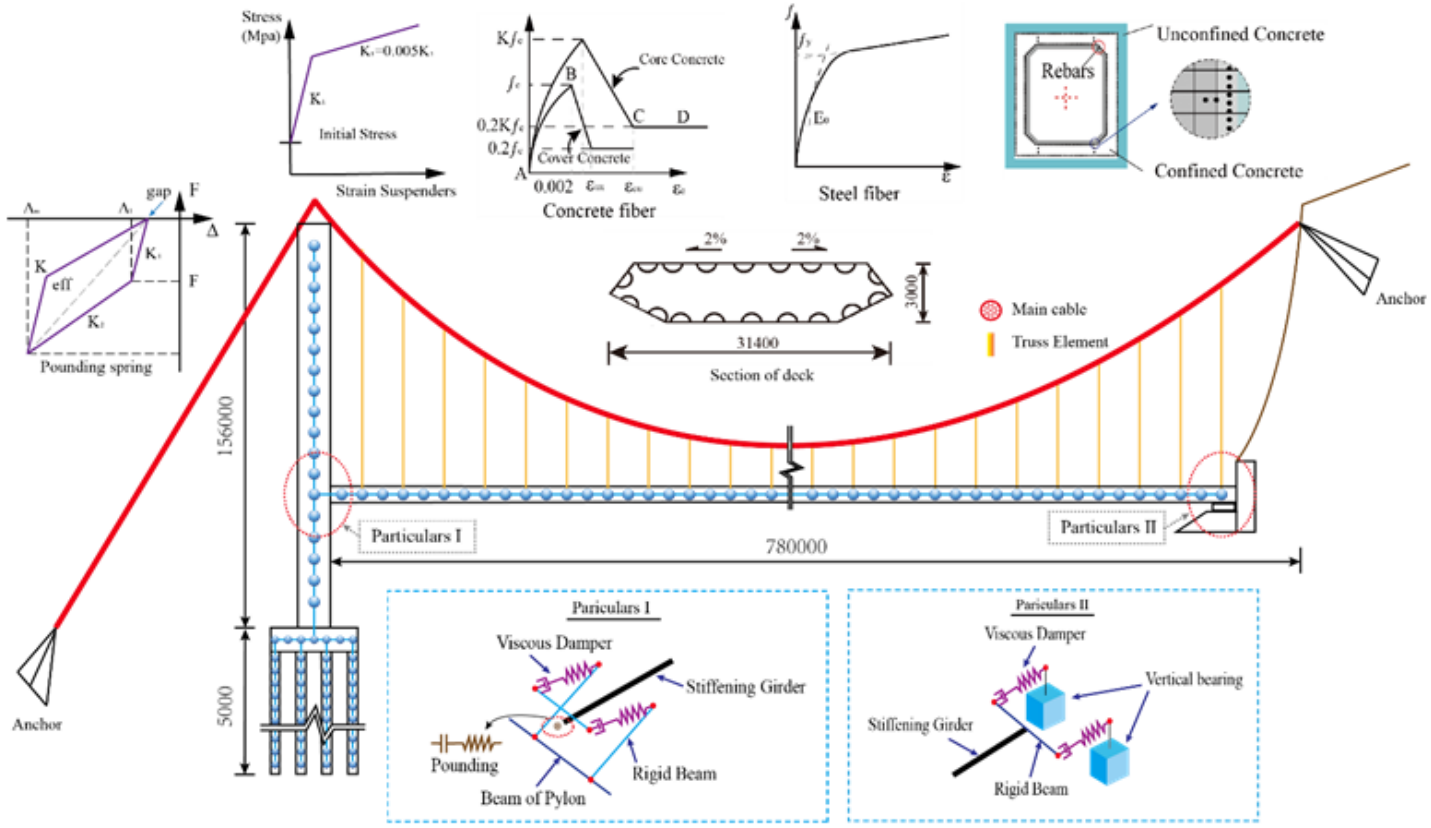

Figure 8

Finite element model of the bridge

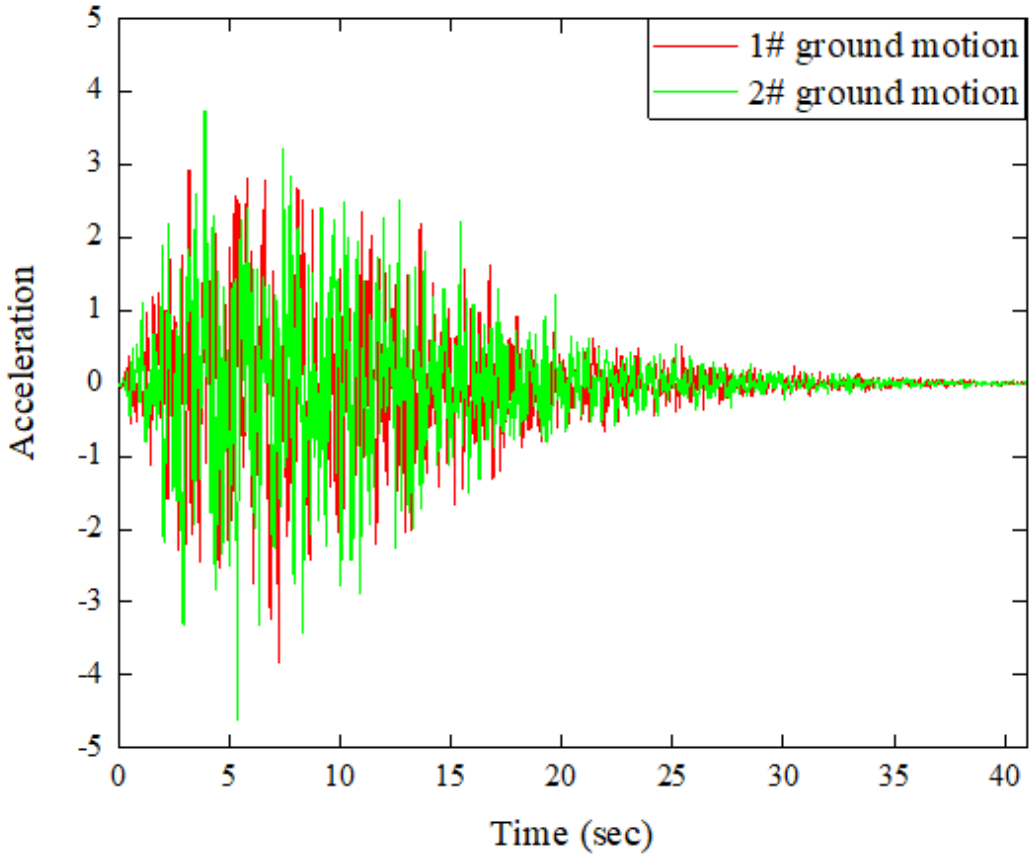

Figure 9

Ground motion sample

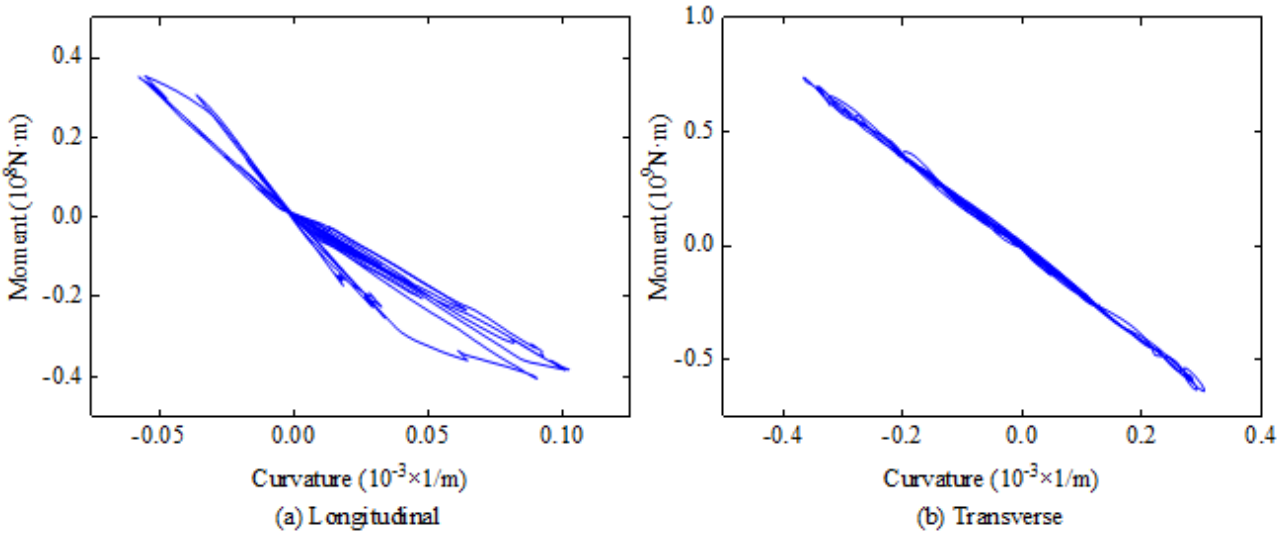

Figure 10

Thebottom section hysteretic curve of pylon

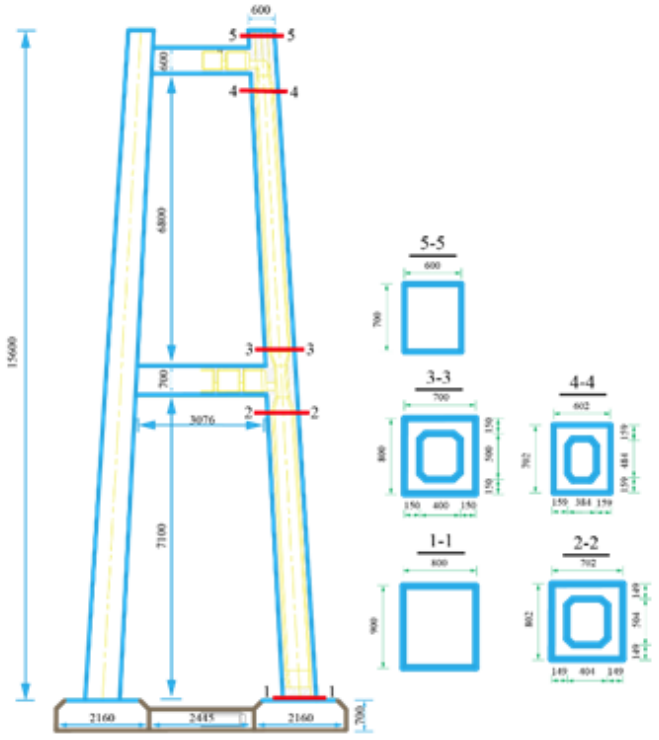

Figure 11

Criticalsection of the pylon

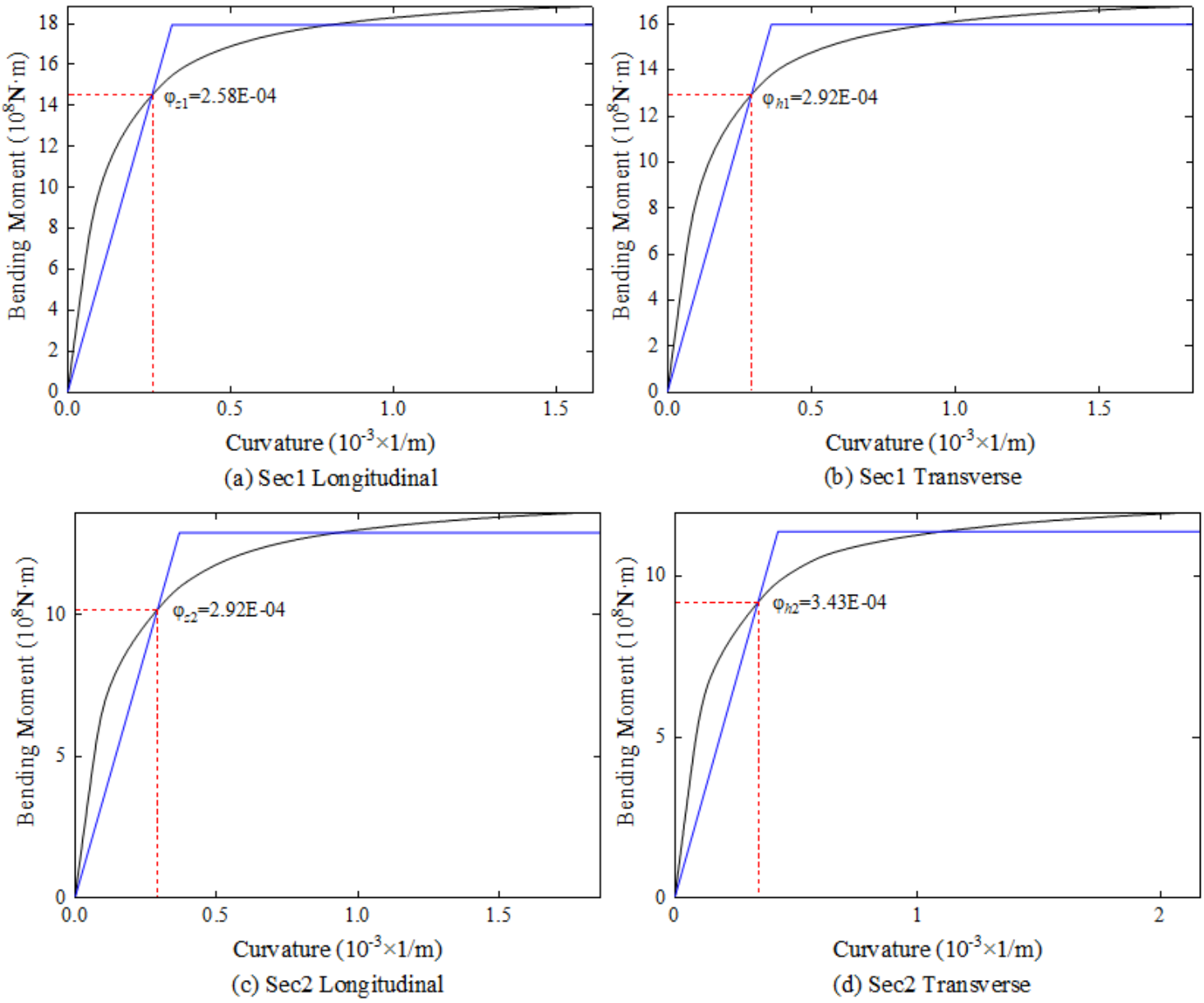

Figure 12

Relationship between bending moment and curvature of bridge pylonat section 1 and section 2

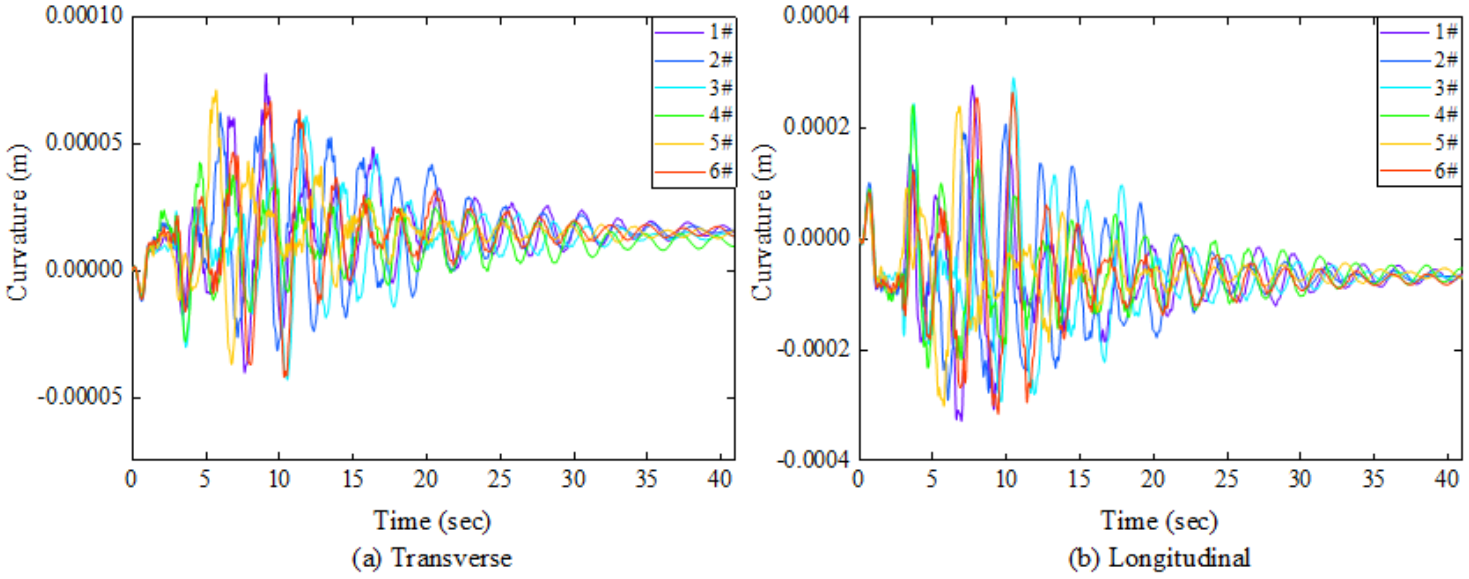

Figure 13

Response of section 1-1 under sample ground motion.

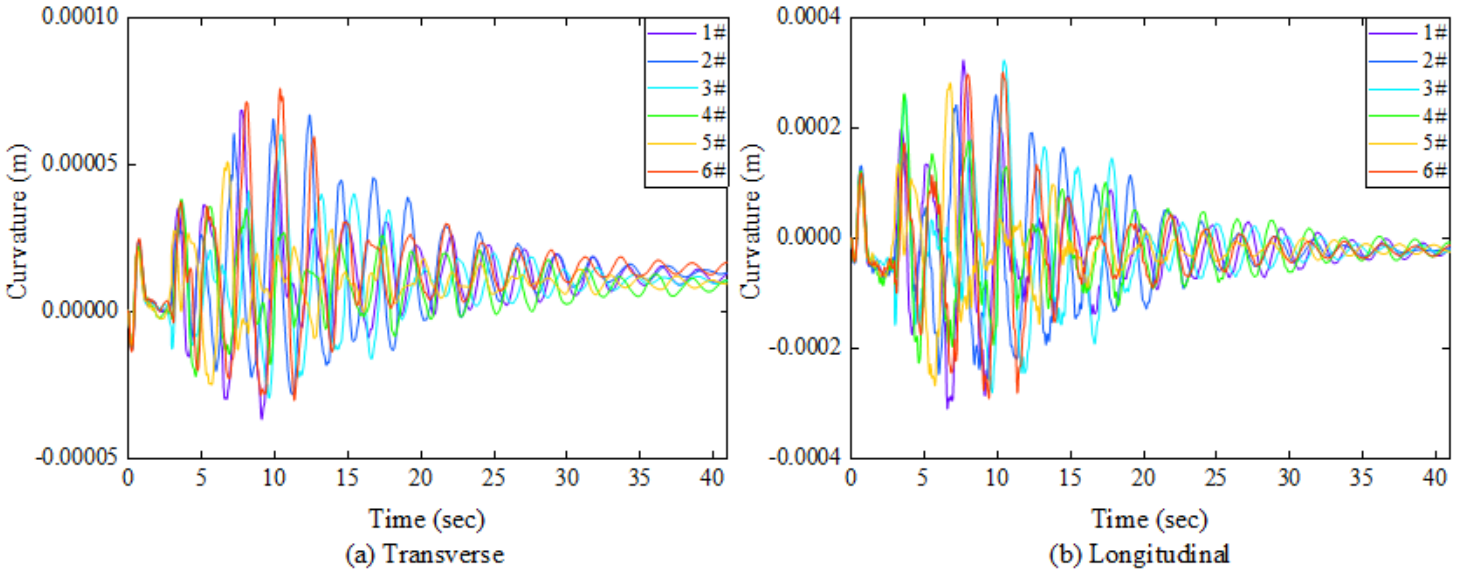

Figure 14

Response of section 2-2 under sample ground motion.

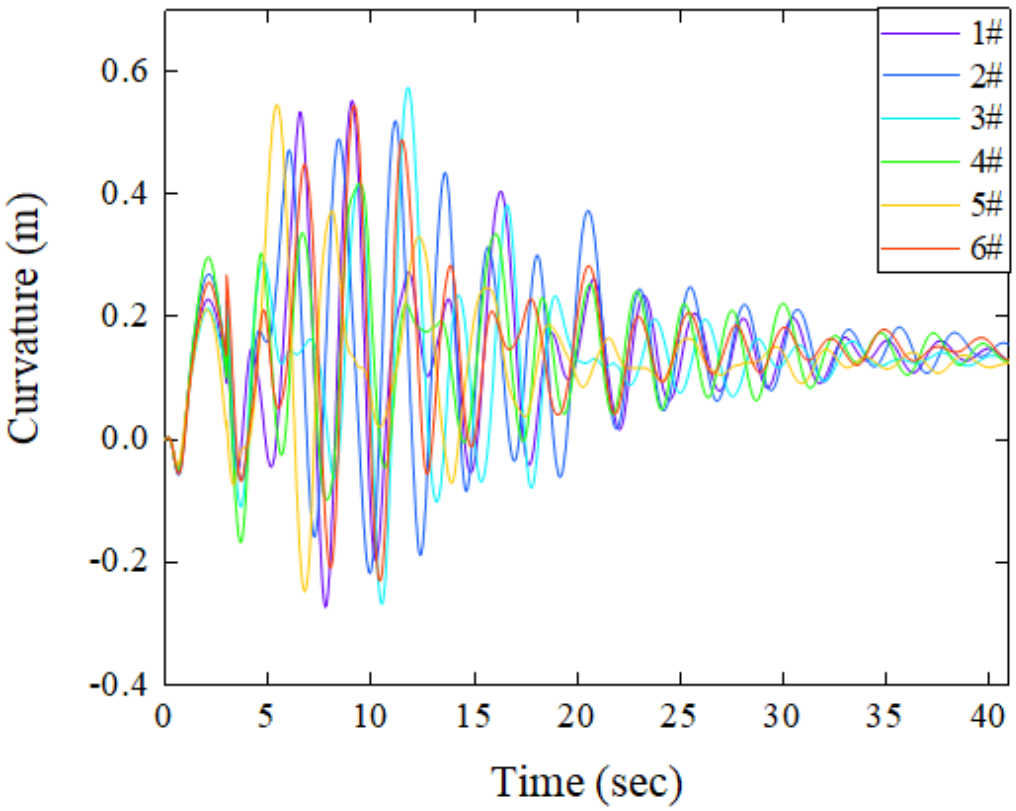

Figure 15

Bearing response under sample ground motion.

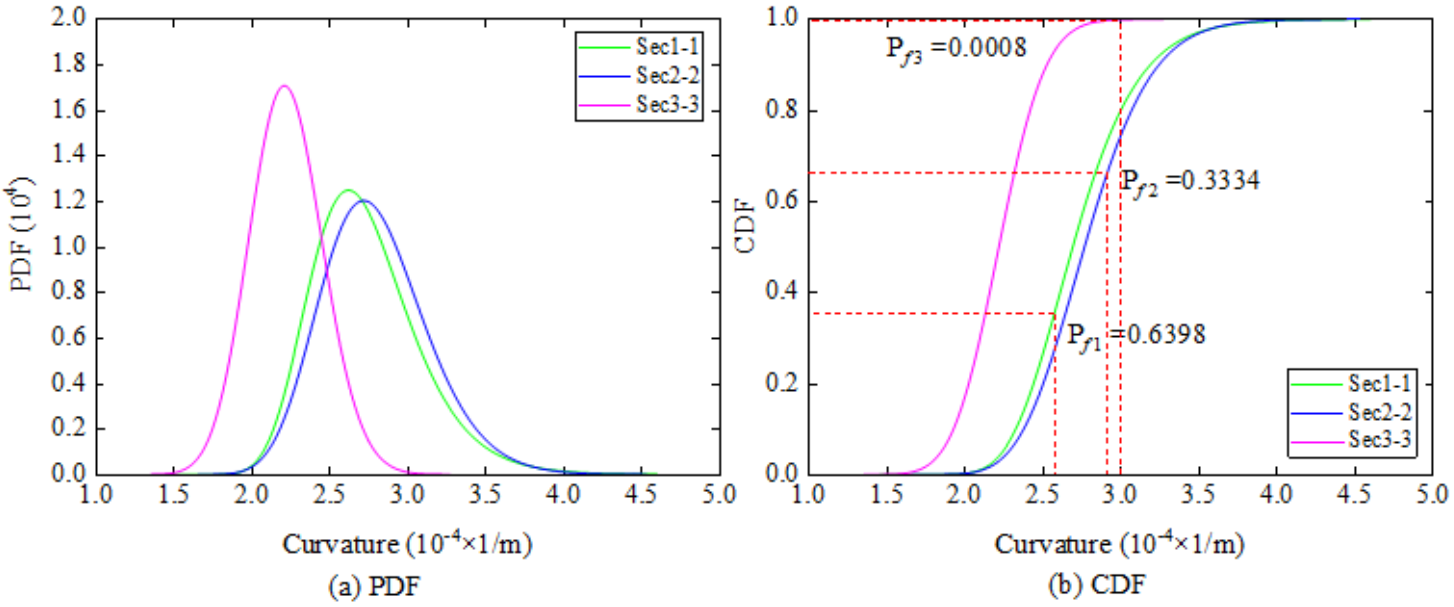

Figure 16

PDF and CDF of 1-1, 2-2, 3-3 longitudinal sections of the bridge pylon

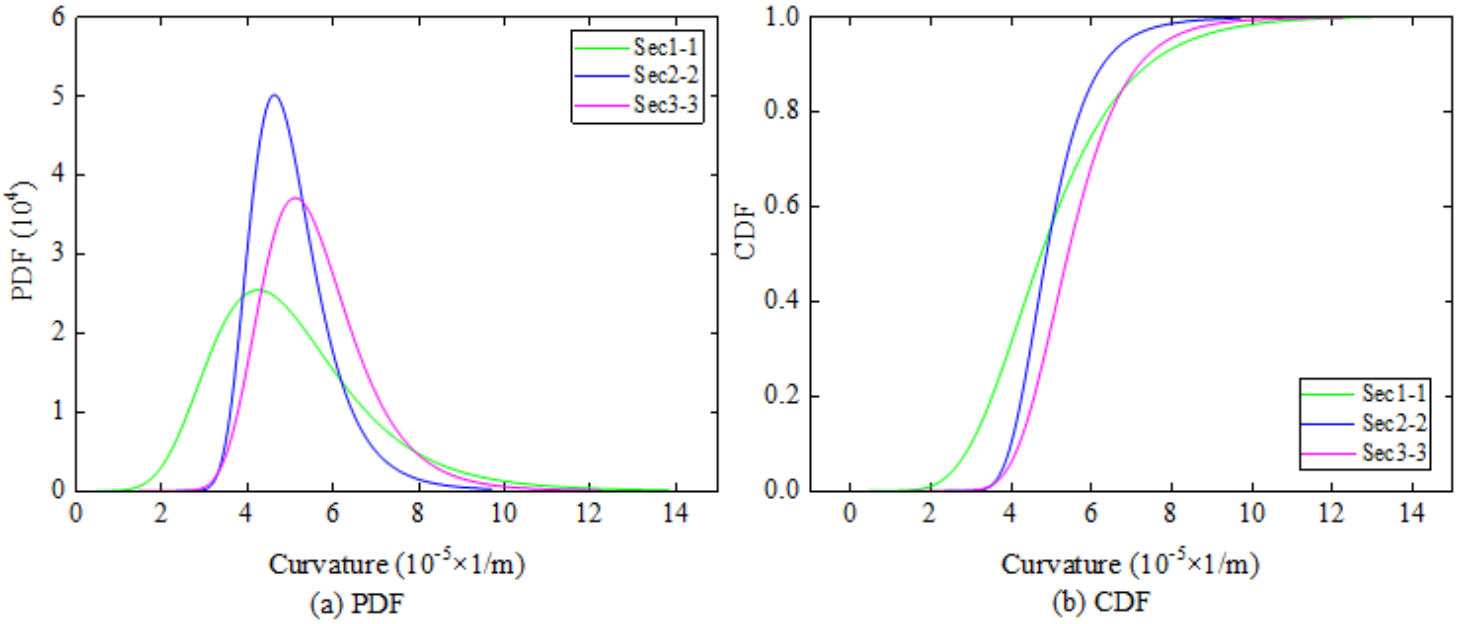

Figure 17

PDF and CDF of 1-1, 2-2, 3-3 transverse sections of the bridge pylon

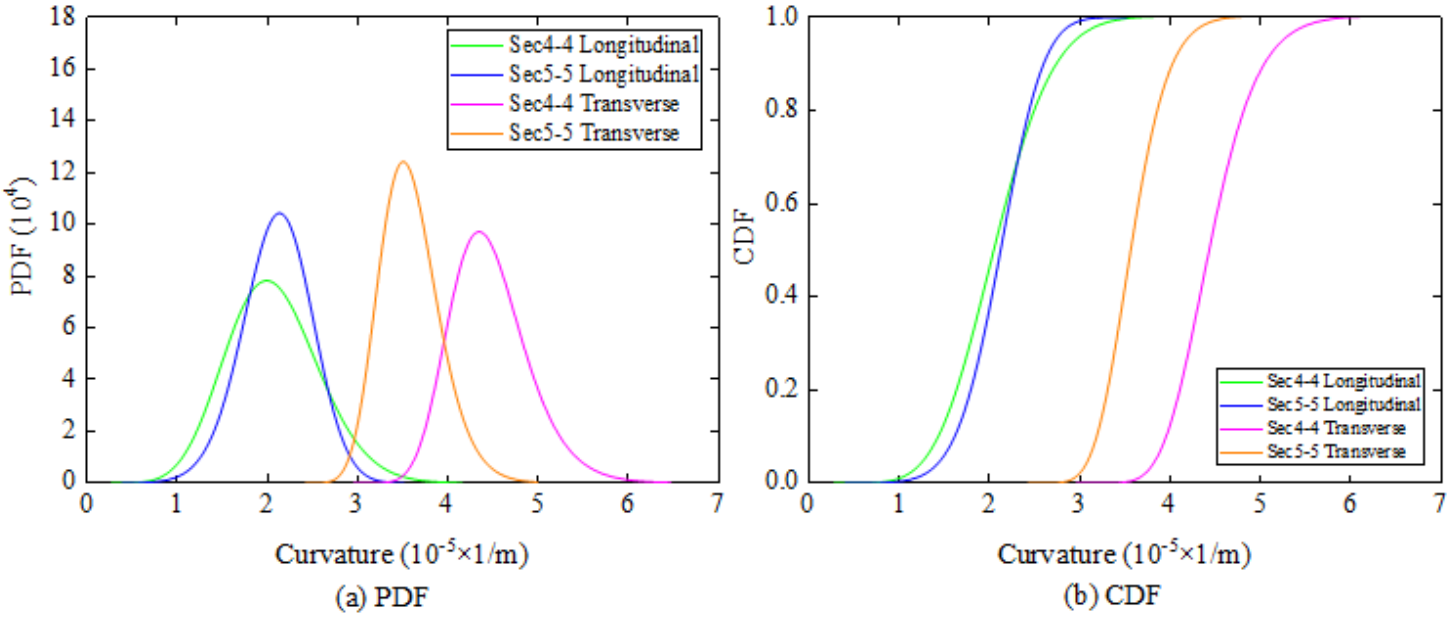

Figure 18

PDF and CDF of 4-4, 5-5 longitudinal and transverse sections of the bridge pylon

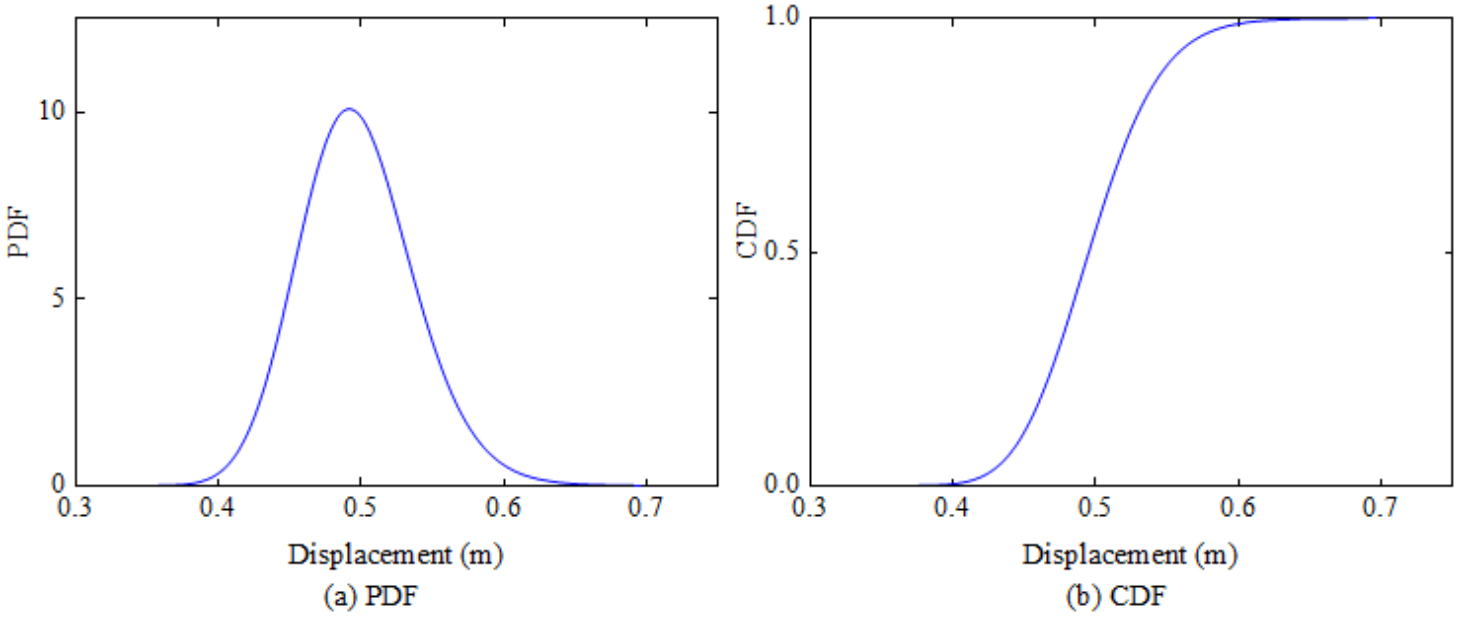

Figure 19

PDF and CDF for bearing